

Modeling Non-Radiative Processes in Solar Materials

by

Alexander Wolfe Kohn

B.S., Harvey Mudd College (2013)

Submitted to the Department of Chemistry
in partial fulfillment of the requirements for the degree of

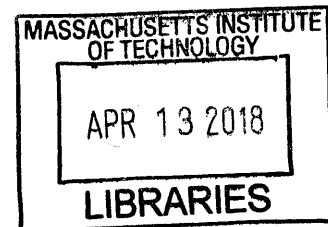
Doctor of Philosophy

at the

MASSACHUSETTS INSTITUTE OF TECHNOLOGY

February 2018

© Massachusetts Institute of Technology 2018. All rights reserved.



ARCHIVES

Signature redacted

Author .

.....
Department of Chemistry
January 19, 2018

Signature redacted

Certified by.....

.....
Troy Van Voorhis
Haslam and Dewey Professor of Chemistry
Thesis Supervisor

Signature redacted

Accepted by

.....
Robert W. Field
Chairman, Department Committee on Graduate Theses



77 Massachusetts Avenue
Cambridge, MA 02139
<http://libraries.mit.edu/ask>

DISCLAIMER NOTICE

Due to the condition of the original material, there are unavoidable flaws in this reproduction. We have made every effort possible to provide you with the best copy available.

Thank you.

The images contained in this document are of the best quality available.

This doctoral thesis has been examined by a Committee of the Department of Chemistry as follows:

Professor Adam Willard **Signature redacted**

Chairman, Thesis Committee

Assistant Professor of Chemistry

Professor Troy Van Voorhis **Signature redacted** ...

Thesis Supervisor

Haslam and Dewey Professor of Chemistry

Professor Jianshu Cao **Signature redacted**

Member, Thesis Committee

Professor of Chemistry

Modeling Non-Radiative Processes in Solar Materials

by

Alexander Wolfe Kohn

Submitted to the Department of Chemistry
on January 19, 2018, in partial fulfillment of the
requirements for the degree of
Doctor of Philosophy

Abstract

In this thesis, we investigate methods and systems for understanding the electronic properties of a variety of systems relevant to organic photovoltaics.

The second chapter examines how to predict the radiative and non-radiative decay rates of a large family of naphthalene derivatives. Naphthalene is a common building block in many organic electronic devices and possesses complex photophysics that are difficult to capture. Principally using time-dependent density functional theory, we are able to reproduce the experimental rates and, moreover, the fluorescence quantum yield, quite accurately.

The next chapter then goes into extensions of the methodology discussed and analyzed in the prior chapter. Anthracene derivatives used for transferring triplet energy between a quantum dot and rubrene phase are found to have varying impacts on the total transfer efficiency based on the triplet lifetime of the anthracene derivative. Most potently, significant spin-orbit coupling in some of the derivatives causes substantial deactivation. An additional family, BODIPY dyes, is also investigated. They are found to undergo internal conversion gated by an excited-state conformational change, suggesting this may be a common motif.

The fourth and fifth chapters investigate different interfacial effects and their impacts on the energy levels of electrons and holes in disordered organic devices. They look at specific systems: the interface between three different donors, PPV, P3HT, PTB7, and PCBM. They find that the interface can both reduce and induce disorder in different systems and that full treatment of the electronic environment is important for capturing accurate results.

The final chapter investigates the use of neural networks to predict optimal range-separation parameters for density functionals.

Thesis Supervisor: Troy Van Voorhis

Title: Haslam and Dewey Professor of Chemistry

Acknowledgments

*Perhaps the true science we did
is the friends we made along the way.*

Contents

1	Introduction	21
1.1	raison d'être	21
1.2	Density Functional Theory	22
1.3	Molecular Mechanics	24
2	Understanding Quantum Yields: Naphthalene Derivatives	27
2.1	Introduction	27
2.2	Computational Details	31
2.2.1	Spin-Orbit Coupling	33
2.2.2	Framework	33
2.3	Results and Discussion	35
2.3.1	Emission Energies and Rates	35
2.3.2	Direct Intersystem Crossing (ISC) and Internal Conversion (IC)	36
2.3.3	Internal Conversion	37
2.3.4	Intersystem Crossing	41
2.3.5	Quantum Yield Evaluation	42
2.4	Conclusion	44
3	Understanding Quantum Yields: Anthracene Derivatives and BOD- IPY Dyes	45
3.1	Anthracene Derivatives	45
3.1.1	Introduction	45
3.1.2	Results	47

3.2	BODIPY Dyes	50
3.2.1	Introduction	50
3.2.2	Preliminary Results	52
4	Carrier Levels in Disordered Organic Photovoltaics: PPV and P3HT	55
4.1	Introduction	55
4.2	Computational Details	59
4.2.1	Molecular Dynamics	60
4.2.2	Electronic Structure Calculations	61
4.3	Results and Discussion	64
4.4	Conclusion	69
4.5	Supporting Information	70
4.6	Acknowledgements	71
5	Carrier Levels in Disordered Organic Photovoltaics: PTB7	73
5.1	Introduction	73
5.2	Computational Details	74
5.2.1	Molecular Dynamics	75
5.2.2	Electronic Structure Calculations	76
5.3	Results and Discussion	77
5.4	Conclusion	79
5.5	Acknowledgements	80
6	Optimal Tuning in Machine Learning	81
6.1	Introduction	81
6.2	Methods	82
6.3	Results and Discussion	82
6.4	Conclusions	85
7	Conclusion	87

List of Figures

2-1	Intersystem crossing (ISC) and internal conversion (IC) processes proposed in the present study. (a) Direct ISC/IC for which the final state is the lowest one with the given multiplicity (S_0 and T_1). (b) Indirect ISC/IC that allows a conformational change of S_1 as the first step. (c) Indirect $S_1 \rightarrow T_{n \geq 2}$ ISC.	31
2-2	Molecules for which the quantum yields are evaluated in the present study are represented by their substitutes. Family I (# 1–12) includes naphthalene and its derivatives and Family II (# 13–27) consist of 1-aminonaphthalene and its derivatives.	32
2-3	Comparison between the theoretical and experimental values for (a) fluorescence energies (E_{fl}) and (b) fluorescent rates (k_{fl}) for Kasha emissions. The dashed lines illustrate the situation where theoretical and experimental values agree with each other.	36
2-4	Energy gap law correlations between the total non-radiative rates (k_{nr}) and (a) the adiabatic energy gaps ($\Delta E_{IC}^{(0)}$) or (b) the reorganization energies ($\lambda_{IC}^{(0)}$) for the $S_1 \rightarrow S_0$ direct internal conversion (IC) from experimental measurements, as well as correlations between the total non-radiative rates (k_{nr}) and (c) the adiabatic energy gaps ($\Delta E_{ISC}^{(1)}$) or and (d) the reorganization energies ($\lambda_{ISC}^{(1)}$) for the $S_1 \rightarrow T_1$ direct intersystem crossing (ISC) from theoretical calculations.	38
2-5	Energy gap law correlations between the total non-radiative rates (k_{nr}) and the (a) experimental or (b) theoretical activation energies.	39

2-6	A plot (a) of the potential energy surfaces along the internal conversion reaction coordinate for the ground state (S_0), first excited singlet (S_1), and second excited singlet (S_2) of 1AN. Above the graph, geometries and transition densities for the S_1 state near the Franck-Condon-region S_1 minimum and at the transition state on the S_1 surface are shown. .	40
2-7	Additionally,	41
2-8	Comparison between theoretical intersystem crossing rate (Family I) or theoretical internal conversion rate (Family II) and experimental nonradiative rate.	42
2-9	Comparison between theoretical and experimental values of quantum yields.	43
3-1	(a) Schematic of the energy transfer in this hybrid photon upconversion platform. Upon excitation with a 488 nm cw laser, triplet energy transfer (TET) occurs from CdSe nanocrystals (NCs) to the bound anthracene transmitter, and subsequently to 9,10-diphenylanthracene (DPA, yellow box). Two DPA triplets fuse to form a singlet, followed by emission at 430 nm. (b) Illustration of TET from CdSe NCs to bound anthracene ligands through anchoring groups, X. The absorption (solid line) and emission (dashed line) spectra of (c) 2.4 nm diameter CdSe NCs, (d) DPA, and (e)-(m) transmitter ligands with different anchoring groups measured in hexane at room temperature.	46
3-2	Plot of the photon upconversion QY for anthracene ligands (yellow bars), simultaneously shown with the relative decrease of initial exciton bleach of the CdSe NC donor (?XB, red triangles, left), and the TET efficiency ?TET (blue squares, right).	47

3-3	The energetics of the reaction path on the T1 surface of An-Py going from the T1 minimum-energy geometry to the T1/ S0 minimum-energy crossing point geometry, as computed using nodes and the freezing string method. ⁴⁵ The first node is at the global minimum and the final node is at the intersection between the T1 and S0 potential energy surfaces. The lower-left structure displays the geometry of An-Py near the global minimum (node 1 on the reaction path above); the lower-right structure is of the local minimum near the minimum-energy crossing point (node 16 on the reaction path above) with the S0 surface, only 0.20 eV above the global minimum. This local minimum seems to be caused by steric clashing between the ortho hydrogens on the aryl groups and the hydrogens in the 1 and 8 positions on the anthracene. This local minimum on the T1 surface can confine the anthracene near a T1/S0 conical intersection, accelerating intersystem crossing between the two states and lowering the triplet lifetime.	49
3-4	The set of BODIPY dyes investigated in Duran-Sampedro, et. al. . .	51
3-5	Plot of the experimental fluorescence energy versus the experimental non-radiative rates. The points in blue are species 1-10, bearing a phenyl group on the 8-carbon. The points in red are species 11-17, bearing a methyl group on the 8-carbon.	53
3-6	Plot of the reaction path of BODIPY dye 1, which has a phenyl group on the 8-carbon and no chlorination.	54

- 4-1 Schematic representing current state of studies on interfacial hole states in polymer-fullerene BHJ devices. The upper left diagram represents the hole state of an ordered polymer *in vacuo*. Some studies have investigated and elaborated on the role of the electronic environment near the interface (top right) [1, 2, 3]. Others have examined disorder of the polymer chain and how that impacts the energetics and spatial extent of the hole state (bottom left) [4, 5]. Herein, we examine both in a realistic system in order to evaluate how the two balance one another (bottom right). 56
- 4-2 Images of the interfaces of (a) PPV/PCBM and (b) P3H PCBM and their dihedral angle distributions, (c) and (d) respectively. The dihedral angle distributions are separated based on their distance from the PCBM interface - red for the closest layers, purple for the farthest. 57
- 4-3 The impact of different interfacial contexts on the band structures. A dielectric mismatch in which the acceptor phase has a larger dielectric than the donor phase (left) causes the bands of the donor phase to become stabilized and the bands of the acceptor phase to become destabilized as the hole and electron become better and worse solvated, respectively. Interfacial disorder (center) disrupts conjugation, confining and destabilizing the hole and electron states. A static interfacial electric field (right) stabilizes the electrons and destabilizes the holes in one domain (depicted here as the donor phase), and destabilizes the electrons and stabilizes the holes in the other. 63

4-4	The band structures at the PPV-PBCM interface (left) and the P3HT-PCBM interface (right) with differing treatments of the environment: as vacuum (red); static point charges (blue); or as static point charges with Drude particles (green). In both systems, inclusion of polarization effects dramatically changes the band structure. Each point has been averaged from 102 calculations and has a standard deviation of 0.05 eV. The distances are resolved by binning each molecule into a layer and using the average distance from the interface of that layer. . . .	63
4-5	The normalized inverse participation ratios (NIPR) for the holes states in the electron-donating polymers being considered, PPV and P3HT. The NIPR was computed for each system with the environment treated as vacuum (red); static point charges (blue); and as static point charges with Drude particles (green). In PPV (left), the extent of delocalization of the hole states shows little influence from the interface, irregardless of the environmental treatment. In P3HT (right), the hole states are more localized near the interface than the bulk, with this effect strengthening as the environment is treated with greater sophistication. ach point has been averaged from 102 calculations and has a standard deviation of 0.01. The distances are resolved by binning each molecule into a layer and using the average distance from the interface of that layer. . . .	67
5-1	The base repeating unit in PTB7. The moiety on the left is relatively electron-poor, whereas the moiety on the right is relatively electron-rich.	75
5-2	Graph of the IP values in PTB7 as a function of distance from the interface in PCBM. Data computed absent of the molecular environment is labeled 'gas' and is red for the hole and blue for the electron. Data computed with the surrounding molecules represented by their point charges is labeled 'point charges' and colored green for the hole and magenta for the electron.	77

5-3	Graph of the EA values in PTB7 as a function of distance from the interface in PCBM. Data computed absent of the molecular environment is labeled 'gas' and is red for the hole and blue for the electron. Data computed with the surrounding molecules represented by their point charges is labeled 'point charges' and colored green for the hole and magenta for the electron.	78
5-4	Graph of the IPR values for the states in PTB7 as a function of distance from the interface in PCBM. Data computed absent of the molecular environment is labeled 'gas' and is red for the hole and blue for the electron. Data computed with the surrounding molecules represented by their point charges is labeled 'point charges' and colored green for the hole and magenta for the electron.	79
6-1	Plot comparing the predicted ω values with the exact ones. We reproduce the true optimal values with a mean absolute error of 0.015 bohr ⁻¹	83
6-2	The distribution of true omega values for the two databases employed in this study. We find that they have little overlap, demonstrating how each one only samples a limited region of ω space.	84
6-3	The distribution of true omega values for the two databases employed in this study, plotted versus the molecule's characteristic radius.	85

List of Tables

3.1 TDDFT calculations were performed at the S0, T1, and S1 geometries, optimized on the DFT or TDDFT potential energy surfaces, respectively. These calculations were performed with the wB97x-D3 functional,¹⁶ a 6-31G* basis, and the Tamm-Dancoff approximation in the case of the TDDFT calculations. Calculations were performed with QChem 4.4 48

4.1 Calculated transport properties for PCBM, PPV, and PCBM. The ionization potential (IP) and electron affinity (EA) have been calculated for the bulk phase of the three materials and with the three environmental treatments being considered. The transition gap (TG) is computed as $E_{IP} - E_{EA}$. Improved treatment of the environment brings theoretical values in line with experimental values. Each value has a standard deviation of 0.05 eV. 62

Chapter 1

Introduction

1.1 raison d'être

A majority of the physical sciences has been directed towards the manipulation of energy for a while now. How to obtain it, how to store it, how to change it - all of these questions lack quick, easy answers. It's difficult to overstate the breadth of the problem - it pervades politics (both local and global) and impacts all technologies.

The existing fossil-fuel-based paradigm has done much, but has limitations. Most pressingly, the effects of climate change are becoming more and more self-evident. Solar energy is the most promising way forward due to its ubiquity and quantity. However, with the development of hydraulic fracturing technology solar energy has fallen well behind natural gas in cost-efficiency. Given that a carbon tax is unlikely to be implemented anytime soon, we need to look for technological solutions. This thesis is dedicated to improving the efficiency of solar devices.

The first step in the conversion of sunlight to electrical energy is the absorption of light by a chromophore. From there, the exciton somehow needs to form charge carriers separated by a voltage differential. In this thesis, the first and second chapters focus on modeling radiative and non-radiative decay processes of the sorts that are relevant in organic photonic devices. The third and fourth chapters examine the energy levels of interfacial charge carriers in bulk heterojunction devices, a common form of organic solar cell. The fifth chapter looks into the use of machine learning to

predict optimal range separation values for use in range-separated hybrid functionals, necessary for accurate outcomes when looking at the excited-state electronic structure of organic molecules.

In this section we will look at some of the tools use in the upcoming chapters whose familiarity to the reader is assumed. These are the defining tools of our field and will be used throughout the following chapters.

1.2 Density Functional Theory

Density functional theory is the most commonly used approach to solving the many-body electronic structure problem. Although, as will show up later, relativistic effects are important, explicitly solving the many-body relativistic electronic structure problem is intractable, and so we will rely on the standard non-relativistic Schrödinger equation:

$$\hat{H}\Psi(r_1, r_2, \dots, r_N, R_1, R_2, \dots, R_M) = E\Psi(r_1, r_2, \dots, r_N, R_1, R_2, \dots, R_M) \quad (1.1)$$

where \hat{H} is the Hamiltonian operator, E is the energy, and Ψ is the "wavefunction" associated with that energy. The wavefunction is a complicated object that defines the current state of the system and is a function of the electronic positions (r_i) and the nuclear positions (R_j). The Hamiltonian operator defines all of the physical interactions in the system. In atomic units ($\hbar = 1$, $q_e = -1$, $m_e = 1$, which will be used throughout this work) the electronic-nuclear Hamiltonian can be expressed as:

$$\hat{H} = -\frac{1}{2} \sum_i^N \nabla_i^2 - \frac{1}{2} \sum_j^M \frac{1}{M_j} \nabla_j^2 - \sum_i^N \sum_j^M \frac{Z_j}{r_{ij}} + \sum_i^N \sum_{i'>i}^N \frac{1}{r_{ii'}} + \sum_j^M \sum_{j'>j}^M \frac{Z_j Z_{j'}}{R_{jj'}} \quad (1.2)$$

where i indexes the N electrons and j indexes the M nuclei. The first two terms describe the kinetic energies of the electrons and nuclei, respectively. The last three terms are the Coulomb potentials describing the electron-electron, electron-nuclear, and nuclear-nuclear interactions, respectively. Although the kinetic components are

separable, the Coulomb terms couple all degrees of freedom together, making life difficult.

Fortunately, we can take advantage of the fact that the lightest nucleon, hydrogen, weighs about 1800 times as much as an electron. This means that under most regimes, the electrons move much more rapidly than the nuclei. One consequence of this is that we can assume that from the perspective of the electrons, the nuclei are fixed - or from another perspective, the nuclei travel along the relaxed, adiabatic electronic potential energy surface. This is the Born-Oppenheimer approximation. Thus, we can solve the electronic problem while treating the nuclei as static point charges, producing the electronic Hamiltonian:

$$\hat{H} = -\frac{1}{2} \sum_i^N \nabla_i^2 - \sum_i^N \sum_j^M \frac{Z_j}{r_{ij}} + \sum_i^N \sum_{i'>i}^N \frac{1}{r_{ii'}} \quad (1.3)$$

The nuclear positions here only enter into the equation parametrically.

Although this clearly simplifies the problem, solutions remain difficult. The most basic mean-field solution, Hartree-Fock theory, leaves a great deal wanting in terms of accuracy. And post-Hartree-Fock methods sacrifice much in scaling, memory usage, and ease-of-use. For these reasons we turn to the titular method of the section, density functional theory.

Density functional theory attempts to trade the complicated N-electron wave function (which contains 3N spatial plus N spin variables) for an easier quantity: the total electron density. Attempts to employ the density instead of the wavefunction began early, with Thomas-Fermi-Dirac theory providing forms for all components of the electronic energy by the early 1930s. Unfortunately, the quantitative results were terrible for chemical applications, failing to predict chemical bonding. It wasn't until 1964, when Hohenberg and Kohn proved that the ground state electronic density was a unique functional of the external potential and that it was variational that interest in the chemistry community was piqued.

1.3 Molecular Mechanics

Although DFT is by far the most commonly used electronic structure method due to its good performance-to-cost ratio, it is still too costly for many applications. For example, calculations on molecules of the sort discussed in Chapter 5 (600 atoms) in a minimally acceptable basis set (5200 basis functions) take around 2 hours with 16 cores on the server currently used in the group. Although that is fast enough to perform a geometry optimization, it isn't fast enough for any sort of sampling of a dynamic trajectory. Additionally, if you want to simulate a system that has more than one molecule the scaling goes out of control very quickly. For these reasons, people have developed approximate methods for large systems or long-time simulations. The most important of these is molecular mechanics.

Molecular mechanics approximates the Born-Oppenheimer surface that the nuclei move along. Instead of explicitly calculating the electronic potential through first-principles equations, a semi-empirical form (a force-field) is adopted:

$$E_{elec}(R_1, R_2, \dots, R_M) \cong V_{ff}(R_1, R_2, \dots, R_M) \quad (1.4)$$

One simple, common form for such a force field is:

$$V_{ff} = \sum_i^M \sum_{i'}^M \left[\frac{Q_i Q_{i'}}{r_{ii'}} + 4\epsilon_{ii'} \left(\left[\frac{\sigma_{ii'}}{r_{ii'}} \right]^{12} - \left[\frac{\sigma_{ii'}}{r_{ii'}} \right]^6 \right) + \frac{1}{2} k_{ii'} (r_{ii'} - b_{ii'})^2 \right] + \sum_i^M \sum_{i'}^M \sum_{i''}^M \left[\frac{1}{2} \eta_{ii'i''} (\cos \theta_{ii'i''} - \cos \phi_{ii'i''})^2 \right] \quad (1.5)$$

where Q_i , $\epsilon_{ii'}$, $\sigma_{ii'}$, $k_{ii'}$, $b_{ii'}$, $\eta_{ii'i''}$, and $\phi_{ii'i''}$ are all parameters. The first term in the expression is the effective Coulomb interaction whereby the nuclei interact as ions with effective charges representing the balance between the nuclei and the shielding electrons. The second term is an empirical Leonard-Jones interaction that captures dispersion interactions with a classical 6-12 potential. The third term is an empirical chemical bonding term. The bond is represented as a harmonic potential binding two atoms together. The final term, the three-body term, is the angular term that

structures the geometry of polyatomic molecules with additional harmonic angular potentials. The Coulomb and Leonard-Jones interactions are global (i.e., between all pairs of atoms in theory, although this isn't done in practice). The vibrational and angular terms only contribute to bonded and bonded-to-bonded atoms, meaning that for the vast majority of pairs (or triplets) of atoms they are set to zero.

Chapter 2

Understanding Quantum Yields: Naphthalene Derivatives

2.1 Introduction

In order to rationally design photochemically functional materials we need to understand their non-radiative decay processes. For example, the efficiencies of most organic electronic devices depend directly on the quantum yield of fluorescence[6, 7, 8], defined by the competition between k_r (the radiative rate) and k_{nr} (the non-radiative rate):

$$\Phi = \frac{k_r}{k_r + k_{nr}} \quad (2.1)$$

One instance of this is in organic light-emitting diode (OLED) devices. In OLEDs the total efficiency is directly proportional to the fluorescence quantum yield: if the excitons formed in the devices undergo rapid non-radiative decay, no light is emitted [9]. Similarly, for organic solar cells radiative and non-radiative decay rates determine exciton lifetimes and therefore the fraction of absorbed photons that generate charge carriers [10]. These non-radiative decay rates are important for many other fields: phosphorescent OLEDs[11], bio-labeling [12, 13, 14], photodynamic therapy [15], and laser dyes [16, 17].

To arrive at quantum yield values we need to understand the relevant photo-

physical pathways. For conventional ground-state-singlet organic molecules, common decay pathways to consider are: internal conversion ($S_1 \rightarrow S_0$), intersystem crossing ($S_1 \rightarrow T_1$), electron removal and addition ($S_1 \rightarrow D^+$, $S_1 \rightarrow D^-$), and photochemical isomerizations ($S_1 \rightarrow S_0^*$) [18]. It is challenging to address all of these pathways simultaneously, so we narrow the scope. Herein, we focus on ubiquitous decay channels in organic compounds - internal conversion (IC) and intersystem crossing (ISC).

Historically, discussion of internal conversion and intersystem crossing has been dominated by the energy gap law [19, 20]. When the S_1 state and the acceptor state are sufficiently well separated, the Franck-Condon factors mediating transfer take the form of an exponential in the energy gap between the two levels [19]. The energy gap law thus predicts that the logarithm of the rate of internal conversion is, roughly, anticorrelated with the magnitude of the fluorescence energy:

$$k_{\text{nr}} \propto -E_{\text{fl}} \quad (2.2)$$

where k_{IC} is the internal conversion rate and E_{fl} is the energy of the emitting photon. This is widely used in experimental groups [20, 21, 22, 23, 24, 25].

Substantial progress beyond the energy gap law has been made in the past few decades, as the energy gap paradigm has been found wanting [26]. Crucially, the energy gap law and the very idea of Born-Oppenheimer states fail at conical intersections (CI), regions of phase-space where the electronic potential surfaces meet and the coupling between the states becomes infinite. CIs have been observed to be crucial for a full understanding of internal conversion in a variety of systems, especially in biomolecules where CIs are thought to protect from photodamage [27, 28, 29, 30, 31, 32, 33, 34, 35, 36]. At these meeting-points between potential energy surfaces (PES), coherent transfer can occur on sub-picosecond timescales.

Computational studies examining internal conversion pathways involving CIs have become more prevalent in the last decade. Unfortunately, internal conversion is a challenging process to model analytically because it arises from nuclear motion. Formally,

the rate derived from Fermi’s Golden Rule can be expressed as:

$$k_{\text{IC}} = \frac{2\pi}{\hbar} |H'_{\text{fi}}|^2 \delta(E_i - E_f) \quad (2.3)$$

$$H'_{\text{fi}} = -\hbar^2 \sum_j \left[\langle \Phi_f \Theta_f | \frac{\partial \Phi_i}{\partial Q_j} \frac{\partial \Theta_i}{\partial Q_j} \rangle - \frac{1}{2} \langle \Phi_f \Theta_f | \Phi_i \frac{\partial^2 \Theta_i}{\partial^2 Q_j} \rangle \right] \quad (2.4)$$

where i and f index the initial and final states, Φ is the electronic wavefunction, Θ is the vibrational wavefunction, and Q_j is the j th normal mode. Solving this expression analytically is challenging.

There are two broad categories of solutions to this problem. The first approach is to explicitly account for nuclear motion. Some do this with approximate solutions to Equation 2.4. However, all of these solutions employ a harmonic oscillator model which struggles to account for photophysically important anharmonicities (e.g., they can not find low-energy conical intersections). A more common way to address nuclear motion is to use a real electronic structure potential to run a swarm of non-adiabatic dynamics trajectories [28, 29, 36]. This is simpler, but running the trajectories can be very expensive and the most commonly employed method of running non-adiabatic dynamics, surface hopping, suffers from overcoherence [1]. The second approach constructs static PESs from key geometries of the system of interest (usually minimum energy points on the conical intersection seam) to make qualitative statements about the pathways [30, 33]. This assumes that internal conversion is ergodic and can be treated with equilibrium statistical mechanics, which is not true for all systems [37]. Additionally, the location of a conical intersection is very sensitive to the quality of electronic structure theory, so the calculations are often very expensive. Due to their cost, studies of this sort usually study only a small region of phase space for a single molecule and therefore fail to calibrate the results with comparative analysis.

Studies of intersystem crossing have also advanced substantially in the past decade. Although ISC usually dominates non-radiative dynamics for small molecules (e.g., the triplet quantum yield in naphthalene, $\phi_{\text{T}} \cong 0.75$ [38]), it is a spin-forbidden process that is usually thought to not be responsible for rapid non-radiative decay

(although there are counterexamples, e.g., 1-nitronaphthalene undergoes ISC in 100 fs [39]). Intersystem crossing is easier to model computationally because it is possible to understand spin-orbit coupling (SOC) without nuclear dynamics. This has allowed for the development of time-independent methods under the Condon approximation (the coupling is independent of nuclear position) that are attractive in their simplicity:

$$k_{\text{ISC}} = \frac{2\pi}{\hbar} |H_{\text{SOC}}|^2 \rho(E_i) \quad (2.5)$$

where $\rho(E_i)$ is the density of accepting vibronic states at the energy of the initial state. Computing this vibrational density of states is now the challenging part, as the cost and number of Franck-Condon factors to compute increases dramatically with number of normal modes [40]. Additionally, there is a need in many systems to go beyond the simple Condon approximation, resulting in truly *ab initio* calculations being computationally infeasible. These complications mean most studies only perform qualitative analyses without adequate comparative analysis [41].

Here, we aim to understand the decay processes in two families of naphthalene dyes through the use of density functional theory calculations. We have narrowed our focus to these molecules in order to use empirical models for determining non-radiative rates within a family. The aminonaphthalene species are dominated by internal conversion, which we find can be well explained by transition to a conformer with the amino group out of plane. The other naphthalene species are dominated by intersystem crossing - we can understand the variation in k_{ISC} from the spin-orbit couplings of T_{2-4} . We find the energy gap law wanting in its ability to explain non-radiative rates. With these results, we can reproduce radiative, internal conversion, and intersystem crossing rates with mean absolute errors (MAEs) of 0.38, 0.68, and 0.34 decades, respectively. Combining the predicted values produces quantum yields with a MAE of 0.22 decades and a mean signed error (MSE) of 0.10 decades. This study shows how one can understand and, in theory, tune these ubiquitous decay processes. This provides a pathway for designing species with higher or lower quantum yields of fluorescence, as well as high-throughput screening.

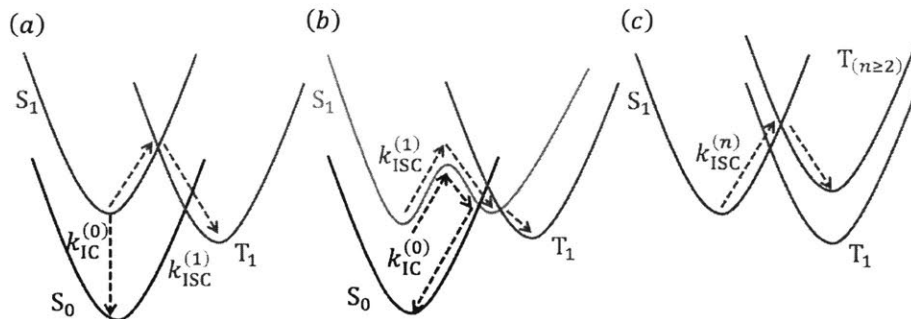


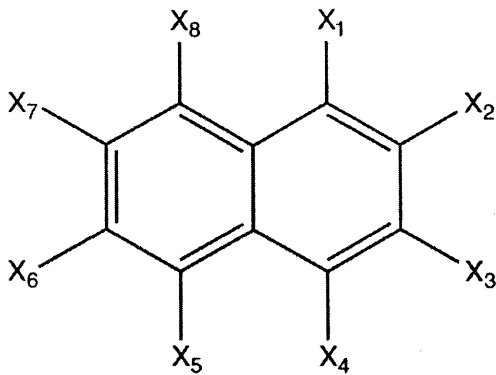
Figure 2-1: Intersystem crossing (ISC) and internal conversion (IC) processes proposed in the present study. (a) Direct ISC/IC for which the final state is the lowest one with the given multiplicity (S_0 and T_1). (b) Indirect ISC/IC that allows a conformational change of S_1 as the first step. (c) Indirect $S_1 \rightarrow T_{n \geq 2}$ ISC.

2.2 Computational Details

In the present study, we focus on two families of molecules: naphthalene and its derivatives (Family I in Fig. 2-2), and 1-aminonaphthalene and its derivatives (Family II in Fig. 2-2). We obtained the experimental k_r 's and k_{nr} 's for Family I from Berlman *et al.*[46] and Family II from the studies performed by Suzuki *et al.*,[43] Takehira *et al.*,[44] and Rückert *et al.*,[45]

We use ground-state density functional theory (DFT) to obtain the S_0 equilibrium molecular geometry and linear-response time-dependent density functional theory (LR-TDDFT) with the Tamm-Dancoff approximation (TDA) for the S_1 geometry [47]. For each molecule, we calculated k_{fl} using Eq. (2.7) based on its E_{fl} and μ_{fl} from LR-TDDFT/TDA at the S_1 -optimized geometry. To help benchmark our methodology, we also calculate the absorption energy, E_{abs} , using LR-TDDFT/TDA at the S_0 geometry.

An earlier CASPT2 study on 1-aminonaphthalene by Montero *et al.* showed that conical intersections play a role in the photophysics of 1AN.[48] Because the conical intersection between two states actually exists in a many-dimensional hyper-seam, it can be difficult to characterize fully [?]. The minimum energy geometry on the seam is one way to characterize the seam and its relevance to, in our case, internal



Family I - naphthalene and derivatives[42]

#	Name	X ₁	X ₂	X ₃	X ₄	X ₅	X ₆	X ₇	X ₈
1	NAPH	H	H	H	H	H	H	H	H
2	1MN	CH ₃	H	H	H	H	H	H	H
3	2MN	H	CH ₃	H	H	H	H	H	H
4	1HN	OH	H	H	H	H	H	H	H
5	2HN	H	OH	H	H	H	H	H	H
6	23DMN	H	CH ₃	CH ₃	H	H	H	H	H
7	26DMN	H	CH ₃	H	H	H	CH ₃	H	H
8	2PN	H	C ₆ H ₅	H	H	H	H	H	H
9	14DPN	C ₆ H ₅	H	H	C ₆ H ₅	H	H	H	H
10	15DPN	C ₆ H ₅	H	H	H	C ₆ H ₅	H	H	H
11	17DPN	C ₆ H ₅	H	H	H	H	H	C ₆ H ₅	H
12	ACN	C ₂ H ₄ -R ₈	H	H	H	H	H	H	C ₂ H ₄ -R ₁

Family II - 1-aminonaphthalene and derivatives[43, 44, 45]

#	Name	X ₁	X ₂	X ₃	X ₄	X ₅	X ₆	X ₇	X ₈
13	1AN	NH ₂	H	H	H	H	H	H	H
14	1A4CNN	NH ₂	H	H	CN	H	H	H	H
15	1A4CLN	NH ₂	H	H	Cl	H	H	H	H
16	1A4MN	NH ₂	H	H	CH ₃	H	H	H	H
17	1MAN	NHCH ₃	H	H	H	H	H	H	H
18	1DMAN	N(CH ₃) ₂	H	H	H	H	H	H	H
19	1DMA4CNN	N(CH ₃) ₂	H	H	CN	H	H	H	H
20	1DMA4CLN	N(CH ₃) ₂	H	H	Cl	H	H	H	H
21	1DMA4MN	N(CH ₃) ₂	H	H	CH ₃	H	H	H	H
22	1DMA4MON	N(CH ₃) ₂	H	H	OCH ₃	H	H	H	H
23	1DMA5MON	N(CH ₃) ₂	H	H	H	OCH ₃	H	H	H
24	1DMA6MON	N(CH ₃) ₂	H	H	H	H	OCH ₃	H	H
25	1DMA7MON	N(CH ₃) ₂	H	H	H	H	H	OCH ₃	H
26	1NAZN	<i>N</i> -azetidinyl	H	H	H	H	H	H	H
27	1NPYN	<i>N</i> -pyrrolidinyl	H	H	H	H	H	H	H

Figure 2-2: Molecules for which the quantum yields are evaluated in the present study are represented by their substitutes. Family I (# 1–12) includes naphthalene and its derivatives and Family II (# 13–27) consist of 1-aminonaphthalene and its derivatives.

conversion. To find it, we use the penalty-function method proposed by Levine *et al.*, selecting $\gamma = 0.02$ Hartree)[49] and implemented by Zhang *et al.*[50].

However, our principal tool, standard LR-TDDFT, does not properly describe conical intersections as it has an incorrect dimensionality of the CI seam [?]. However, we find that spin-flip time-dependent density functional theory (SF-TDDFT), which does not have the dimensionality problem, is a useful tool for finding regions of increased internal conversion [?]. We use SF-TDDFT to find the aforementioned minimum energy crossing point (MECI) between the S_0 and S_1 states. The energy gaps between the S_1 Franck-Condon minimum and the MECI are presented in the

SI. These gaps can be used to parameterize a linear free-energy relation, reproducing internal conversion rates with a MAE of 0.27 decades. However, SF-TDDFT necessitates the use of exotic functionals (we use BHHLYP, 50% Hartree-Fock and 50% Becke exchange[] with Lee-Yang-Parr correlation[]) []. To anchor our results in more-familiar LR-TDDFT, we construct a reaction path from the Franck-Condon minimum to the MECI geometry using standard TDDFT and the frozen string method []. We then find the transition point on this reaction path, and instead use that to parameterize an Arrhenius-like model.

All DFT calculations discussed in the present section were performed in Q-Chem 4.4 [51] using the ω b97x-D3 functional [?, ?] and the 6-31g* basis set [?]. Common TDDFT functional struggle to accurately reproduce the S_1/S_2 (L_b/L_a) ordering of polycyclic aromatic systems [?]. For example, for plain naphthalene the experimental S_1/S_2 gap is 0.53 eV, while B3LYP inverts the ordering with a gap of -0.09 eV. For this reason, we chose to use ω b97x-D3, which predicts the correct ordering with a gap of 0.32 eV.

2.2.1 Spin-Orbit Coupling

Recent work by Marian and coworkers [?] has expanded the calculation of spin-orbit couplings within the framework of time-dependent density functional theory (TDDFT). We use the one-electron Breit-Pauli Hamiltonian recently implemented in QChem:

$$H_{\text{SO}} = -\frac{\alpha^2}{2} \sum_{i,A} \frac{Z_A}{r_{iA}^3} (\mathbf{r}_{iA} \times \mathbf{p}_i) \cdot \mathbf{s}_i \quad (2.6)$$

where i and A index electrons and nuclei, Z_A is the charge of nucleus A , and \mathbf{s}_i is the spin vector of electron i [].

2.2.2 Framework

The scheme we use computes the elements of the quantum yield separately as follows:

1. Radiative rate (k_r):

- (a) We first optimize the molecule on the lowest excited singlet surface (S_1) using TDDFT.
- (b) At the S_1 geometry, we use TDDFT to calculate the energy gap and transition dipole moment between the S_1 state and the ground state singlet (S_0). We then use these to evaluate the radiative rate using Einstein’s formula for spontaneous emission[52]:

$$k_{\text{fl}} = \frac{4\alpha^3 E_{\text{fl}}^3 |\mu_{\text{fl}}|^2}{3}. \quad (2.7)$$

E_{fl} , μ_{fl} and α are the fluorescent energy gap, the transition dipole moment and the fine structure constant respectively.

We follow Kasha’s rule here - molecules emit from their lowest-energy state of a given multiplicity [53] (in general there are exceptions, but they are rare []). This means that E_{fl} and μ_{fl} become E_{S_1} and μ_{S_1} .

2. Internal conversion rate (k_{IC}):

- (a) From the S_1 -minimized geometry, we find the minimum-energy point on the conical intersection seam between S_1 and S_0 state using spin-flip TDDFT (SF-TDDFT). We then use standard TDDFT to characterize the reaction path and find the transition state between the Franck-Condon region local minimum and the located conical intersection (Fig. 2-1(a)).
- (b) We use the computed activation energies and experimental internal conversion rates to fit the prefactor for an Arrhenius-like ansatz:

$$k_{\text{ic}} = A \exp(-E_{\text{a}}/k_{\text{b}}T) \quad (2.8)$$

3. Intersystem crossing rate:

- (a) At the S_1 -minimized geometry, we compute the SOCs between S_1 and energetically-local triplets.

- (b) We use the computed SOCs and experimental non-radiative decay rates to fit the intersystem crossing rate using the expression:

$$k_{ISC} = B + C \sum_i^{2-4} |H_{\text{SOC}}|_{S_1/T_i}^2 \quad (2.9)$$

Where B and C are fit parameters.

4. Quantum yields

- (a) We compute the quantum yield of fluorescence as:

$$\Phi = \frac{k_{\text{fl}}}{k_{\text{fl}} + k_{\text{nr}}} \quad (2.10)$$

$$k_{\text{nr}} \simeq k_x \quad (x = \text{ISC} \text{ or } \text{IC}). \quad (2.11)$$

in which k_{f} , k_{nr} , k_{IC} , and k_{ISC} are the fluorescence, non-radiative, internal conversion, and intersystem crossing rates, respectively.[54] Equation 2.11 expresses the assumption that one of the two decay processes considered here is dominant. Although we currently choose the dominant pathway based on experimental evidence, we believe that extending our methodology to be fully black-box is viable.

2.3 Results and Discussion

2.3.1 Emission Energies and Rates

To compute the quantum yield of a given we first need an accurate emissive geometry. We employ standard TDA-TDDFT to acquire S_1 geometries that give MAEs in the emission energy of 0.71 eV, shown in Figure 2-3. The mean absolute error of absorption energies is 0.66 eV, with results shown in Plot XXX of the SI. Both of these results are quite poor for TD-DFT, for which we would normally expect MAEs around 0.3 eV. However, as one can see in Figure 2-3, the predicted emission energies are uniformly too high. Simply calibrating our results by subtracting 0.71 eV from

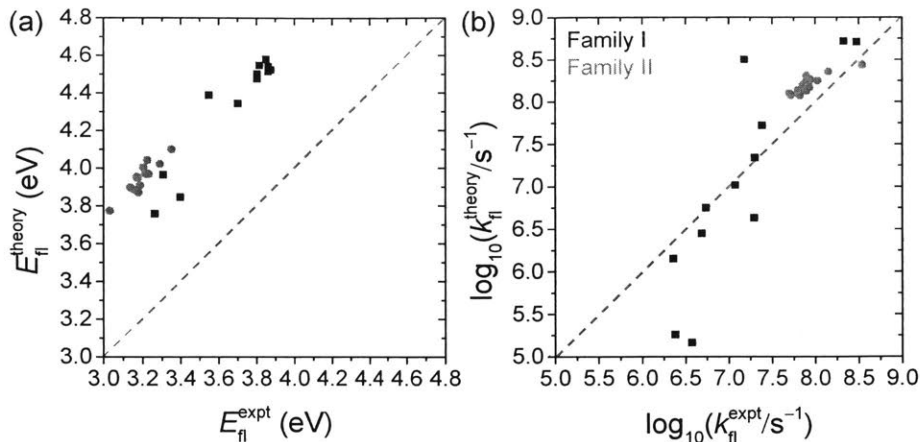


Figure 2-3: Comparison between the theoretical and experimental values for (a) fluorescence energies (E_{fl}) and (b) fluorescent rates (k_{fl}) for Kasha emissions. The dashed lines illustrate the situation where theoretical and experimental values agree with each other.

all values results in a MAE of 0.06, reflecting that our results are qualitatively very accurate.

Having obtained satisfactory emissive geometries, we computed the radiative rate of emission using Equation 2.7. Comparison to experiment is shown in Figure 2-3. While past studies have found that transition dipole moments (TDMs) are challenging for TDDFT to compute [?, ?], we find that for our purposes the calculated TDMs produce acceptable radiative rates, with a MAE of 0.38 decades. Much of the error arises from large underpredictions of the radiative rates of the poorly emissive compounds NAPH and 1MN, possibly a reflecting a need to go beyond the "frozen" Condon approximation.

2.3.2 Direct Intersystem Crossing (ISC) and Internal Conversion (IC)

To evaluate the quality of available correlations for non-radiative decay rates, we looked at the predictive utility of the emission energy (justified via the Energy Gap Law) and the Stokes Shift. Shown plotted in Figure 2-4 (a)-(b) are the reported

experimental non-radiative decay rates as a function of the experimental emission energies and Stokes Shifts. We use as the independent variables experimental photophysical parameters in order to show that the problem is *not* quality of electronic structure theory, but in the energy gap law model.

As discussed in the introduction, conventional models of internal conversion and intersystem crossing often look at direct transfer to the S_0 and T_1 states, respectively. Under the energy gap law assumption, the log of the rate of these non-radiative processes should be linearly anticorrelated with the energy gap. As one can see, if such a correlation is there, it is so weak as to be nearly useless.

We performed a similar analysis for direct ISC by considering $\Delta E_{\text{ISC}}^{(1)}$ and $\lambda_{\text{ISC}}^{(1)}$, plotting their correlation with the experimental k_{nr} 's in Fig. 2-4 (c)-(d). These results indicate the difficulty predicting non-radiative rates using simply the energy gap law.

2.3.3 Internal Conversion

Although internal conversion in the aminonaphthalenes can't be understood as a direct transition from the emissive geometry, we do find that a S_1 to S_0 transition is likely responsible for the decay process. However, this internal conversion is mediated by a transition to a novel conformer. One of the advantages of the aminonaphthalene data set is the availability of activation energies of internal conversion. We plot in Figure 2-5 the activation energy required to reach the transition state from the Franck-Condon local minimum versus the experimental activation energy. We observe that the experimental activation barriers are very good predictors of the experimental rates - the prefactors vary little. And although we slightly overestimate the experimental activation energies, we otherwise capture the energies very well.

As these activation energies predict the internal conversion rates very accurately, we have a method of computing the total non-radiative rates for aminonaphthalenes. A simple linear fit of the logarithm of the rates to the computed activation energies allows us to reproduce the rates with a MAE of 0.68 decades, excellent agreement given that they vary over four decades.

In our interpretation of aminonaphthalene photophysics, internal conversion is

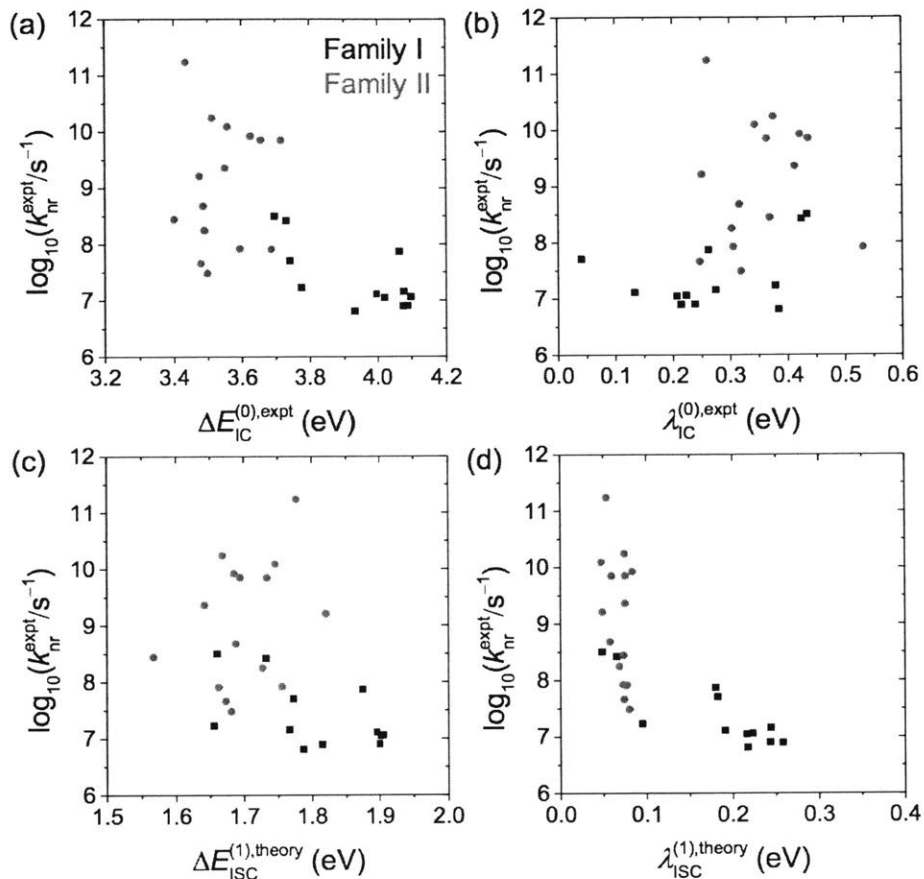


Figure 2-4: Energy gap law correlations between the total non-radiative rates (k_{nr}) and (a) the adiabatic energy gaps ($\Delta E_{\text{IC}}^{(0)}$) or (b) the reorganization energies ($\lambda_{\text{IC}}^{(0)}$) for the $S_1 \rightarrow S_0$ direct internal conversion (IC) from experimental measurements, as well as correlations between the total non-radiative rates (k_{nr}) and (c) the adiabatic energy gaps ($\Delta E_{\text{ISC}}^{(1)}$) or and (d) the reorganization energies ($\lambda_{\text{ISC}}^{(1)}$) for the $S_1 \rightarrow T_1$ direct intersystem crossing (ISC) from theoretical calculations.

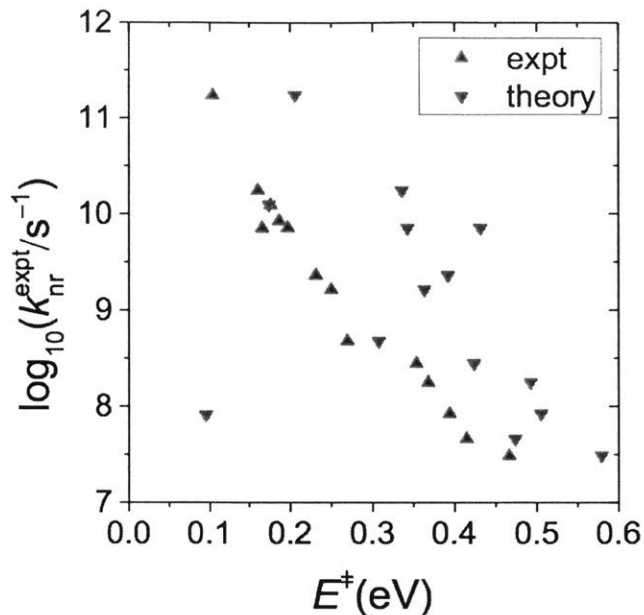


Figure 2-5: Energy gap law correlations between the total non-radiative rates (k_{nr}) and the (a) experimental or (b) theoretical activation energies.

controlled by the transition from the Franck-Condon local minimum conformer to a distorted conformer. In this novel conformer, the amine group and the 1-carbon bonded to it are pulled out of plane nearly perpendicular to the naphthalene core, as shown in figure 2-7. When stretched in this manner, the excitation localizes to the amino group, the 1-carbon, and the 2-carbon.

This mechanism rationalizes trends observed in the aminonaphthalenes. For a given amino substitution, an inverse energy gap law relation is observed: as the emission energy decreases, the internal conversion rate also decreases. This is contrary to conventional wisdom, but can be easily understood in our framework. If internal conversion rates are limited by the activation of a transition state, then under a Bell-Evans-Polanyi model we would suppose that the relative energies of the two basins predict the activation energy [?]. If we assume that the energy of the near-CI region is the same for all species with the same amino substitution (justified by the localization of the excitation near the amino group), then the energy gap would be determined by the height of the near-Franck Condon region, which is also probed by

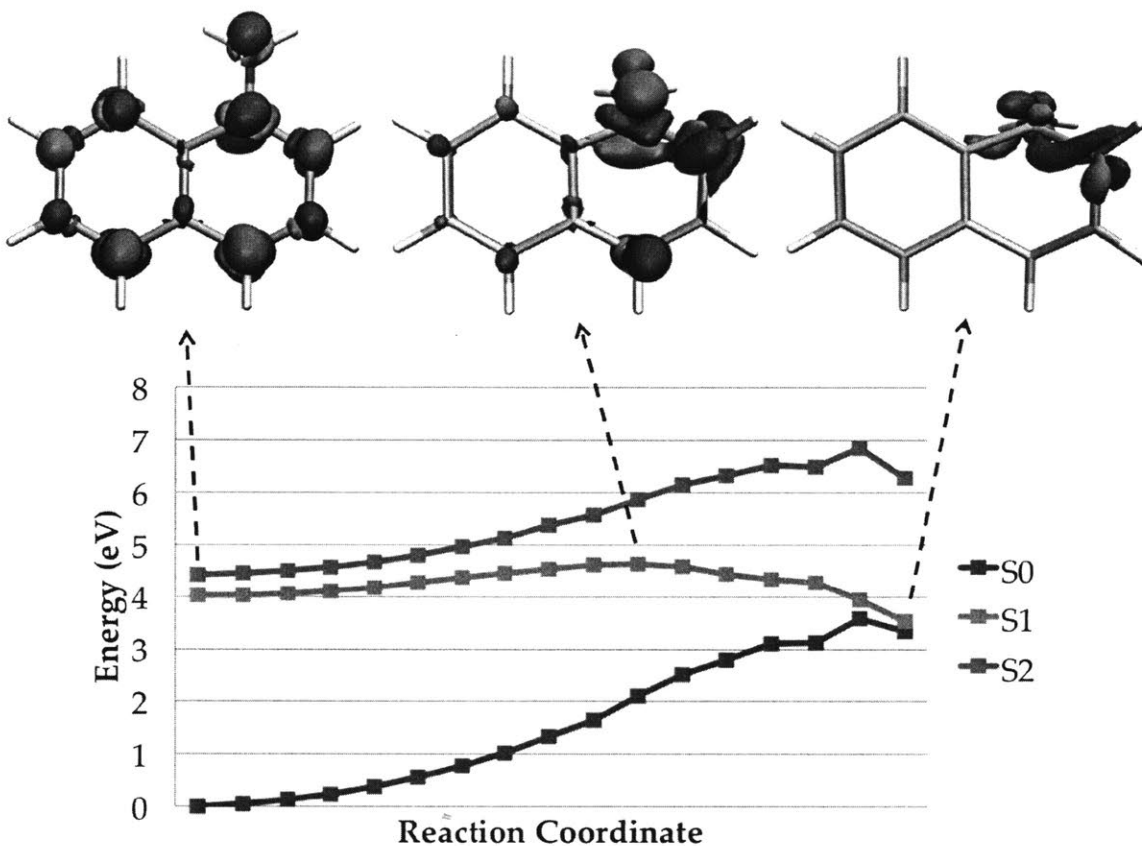


Figure 2-6: A plot (a) of the potential energy surfaces along the internal conversion reaction coordinate for the ground state (S_0), first excited singlet (S_1), and second excited singlet (S_2) of 1AN. Above the graph, geometries and transition densities for the S_1 state near the Franck-Condon-region S_1 minimum and at the transition state on the S_1 surface are shown.

the emission energy. A larger emission energy means that the transition state is more downhill and internal conversion is faster, in opposition to a traditional energy gap model.

The nature of the aminonaphthalene internal conversion pathway has been investigated in several past studies [?]. Most notably, Montero et. al. [] used CASPT2 calculations and concluded that decay proceeded via a S_1/S_2 CI, followed by transfer through an S_2/S_1 CI. However, experimentally they find no evidence for a S_1/S_2 CI being relevant in the photodynamics. Our excellent agreement with experiment shows how using a cheaper, inferior electronic structure method can give one greater

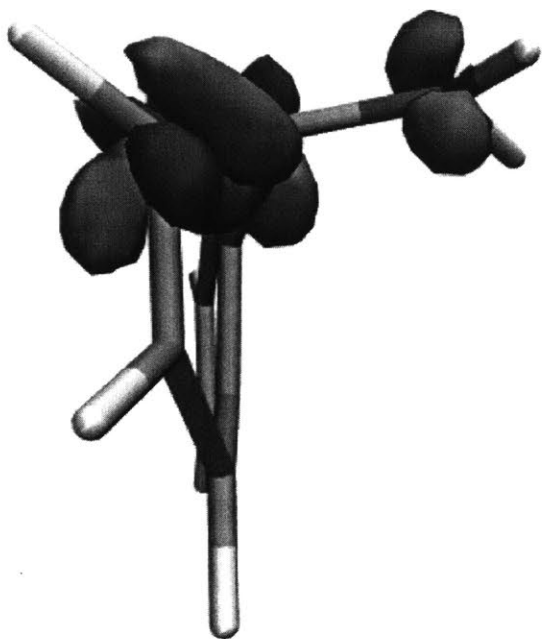


Figure 2-7: Additionally,

insight into photophysical processes.

2.3.4 Intersystem Crossing

Intersystem crossing is ubiquitous in organic small molecules and often is the dominant deactivation pathway. That said, within a family there is usually not much variation in the rate. We find that the intersystem crossing rates for the naphthalenes taken from Berlman [?] are best modeled using a simple semi-empirical rate expression given below:

$$k_{ISC} = A + B \sum_{i=2-4} |H_{SOC-S_1/T_i}|^2 \quad (2.12)$$

where k_{ISC} is the total ISC rate, H_{SOC-S_1/T_i} is the spin-orbit-coupling matrix element between the S_1 (emissive) state and a given triplet state, and A and B are empirically fit parameters. This is a sort of "frozen" Condon approximation, with the additional assumption that T_2 , T_3 , and T_4 are the only photophysically relevant states, and that they additionally have equal acceptor densities of states. We experi-

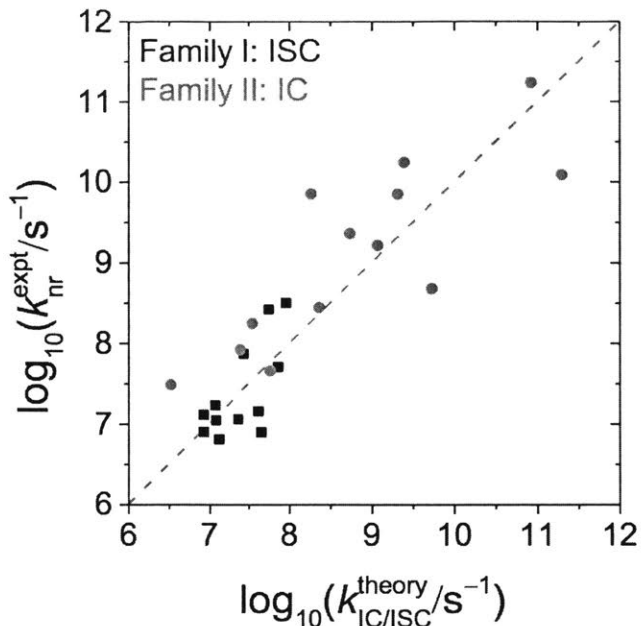


Figure 2-8: Comparison between theoretical intersystem crossing rate (Family I) or theoretical internal conversion rate (Family II) and experimental nonradiative rate.

mented with other forms, similar to Using this form and the data from Berlmán [?], we have solved for A and B as $10^{6.92} \text{ s}^{-1}$ and $10^{7.22} \text{ s}^{-1} \text{ cm}^2$, respectively. We plot the experimental non-radiative rates versus the predicted total k_{isc} in Figure 2-8 (black points). We reproduce the experimental rates with a MAE of 0.34 decades, which, although greater than the experimental errors of 0.06 decades [?], is extremely good.

2.3.5 Quantum Yield Evaluation

With these fits, we can finally evaluate our ability to compute fluorescence quantum yields. We show in Figure 2-9 the correlation between our calculated quantum yields and the experimental quantum yields. We reproduce the experimental values with a MAE of 0.22. As is evident from Figure 2-9, we tend to overestimate the quantum yield - the mean signed error is 0.1 - due to a tendency to overestimate the radiative rate.

We can analyze which components of our predictions are most lacking by com-

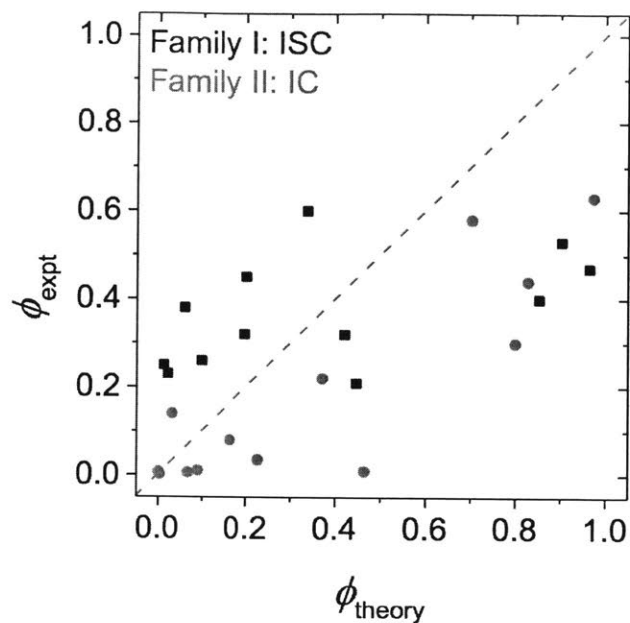


Figure 2-9: Comparison between theoretical and experimental values of quantum yields.

binning predicted radiative rates with experimental non-radiative rates and vice versa. If we use the predicted radiative rates with the experimental non-radiative rates, we compute quantum yields with a MAE of 0.12, which is around the same as experimental error [?]. Similarly, if we use the predicted internal conversion rates of family II with their experimental radiatives rates we arrive at quantum yield MAE of 0.12 which, again, is pretty good. However, combining the predicting non-radiative rates with the experimental radiative rates yields a quantum yield with MAE of 0.16, the worst of the three. This suggests that

2.4 Conclusion

Herein, we have analyzed the components necessary for a calculation of the fluorescence quantum yield. The fluorescence quantum yield is determined from competition between the radiative rate and the various non-radiative rates in the system. We find that TDDFT is an adequate tool to compute the absolute rate of fluorescence, yielding an MAE of 0.38 decades. However, techniques to calculate the absolute rate for nonradiative processes remain wanting. Additionally, even heuristics such as the energy gap law provide little help. Our approach to nonradiative rates is to use semi-empirical fitting. For internal conversion, we use an Arrhenius-like scheme for the transition to a novel conformer, yielding rates with a MAE of 0.68 decades. For intersystem crossing we use a "frozen" Condon scheme in which T_2 , T_3 , and T_4 are all equally accessible, resulting in rates with a MAE of 0.34 decades. Combined, these give us quantum yields with a MAE of 0.22.

The results here show a path for other studies seeking to understand the photo-physics of a family of dyes. They also suggest limitations to the energy-gap law and ways in which an apparent reversal of the energy gap law can occur.

We anticipate future work on families whose photophysical decay pathways are more important, such as the BODIPY dyes. More work into understanding intersystem crossing pathways is also merited, as our understanding evinced here can be improved.

Chapter 3

Understanding Quantum Yields: Anthracene Derivatives and BODIPY Dyes

3.1 Anthracene Derivatives

3.1.1 Introduction

Third generation solar cells can collect more than one charge carrier pair per absorbed photon. One route to this is via triplet excitons. This is because triplet fusion or singlet fission enables photon upconversion or downconversion respectively; processes that can enable devices that exceed the Shockley-Queisser limit. One promising route to triplet capture employs transfer between a quantum dot and a tethered molecular triplet acceptor. Collaborators of ours in Ming Lee Tang's group at the University of California - Riverside investigated the effect of modifying the functional group (X) tethering a molecular triplet acceptor, anthracene, to a CdSe nanocrystal (Fig. 1a and b). Using 9 different functional groups to attach the anthracene acceptor (Fig. 1), they found that the electronic structure of the bridge drastically affected transfer of the triplet exciton.

Their motivation was in part based on binding affinity. Their current workhorse,

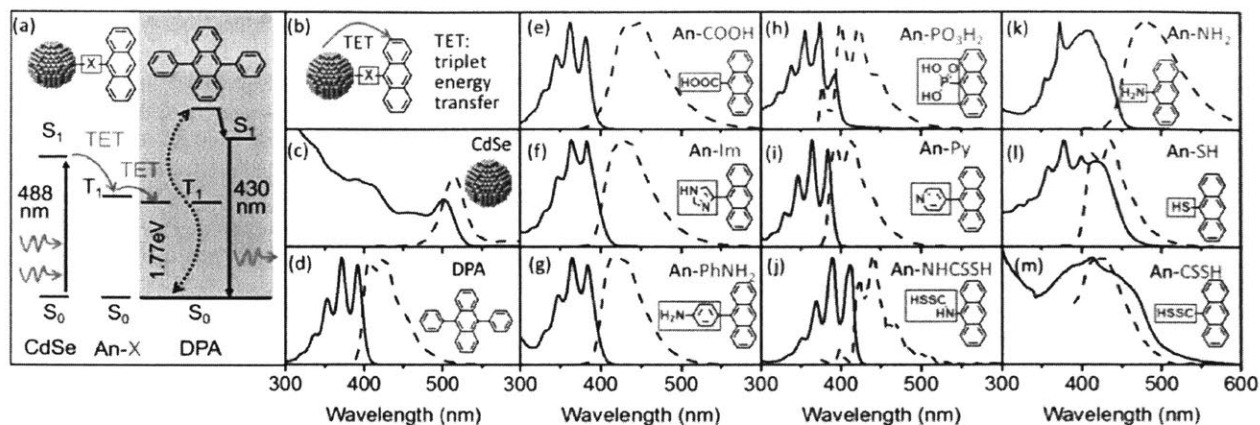


Figure 3-1: (a) Schematic of the energy transfer in this hybrid photon upconversion platform. Upon excitation with a 488 nm cw laser, triplet energy transfer (TET) occurs from CdSe nanocrystals (NCs) to the bound anthracene transmitter, and subsequently to 9,10-diphenylanthracene (DPA, yellow box). Two DPA triplets fuse to form a singlet, followed by emission at 430 nm. (b) Illustration of TET from CdSe NCs to bound anthracene ligands through anchoring groups, X. The absorption (solid line) and emission (dashed line) spectra of (c) 2.4 nm diameter CdSe NCs, (d) DPA, and (e)-(m) transmitter ligands with different anchoring groups measured in hexane at room temperature.

the carboxylic acid functionalized anthracene (An-COOH, Fig. 1e) does not bind very strongly to chalcogenide surfaces ($K_a = 1.3 \times 10^6 \text{ M}^{-1}$). On the other hand, the phosphonic acid functional group (An-PO₃H₂, Fig. 1h) has been shown to bind more strongly to the surface of CdSe NCs than carboxylic acid. Stronger bases or nucleophiles like imidazole, pyridine, aniline, amine (An-Im, An-Py, An-PHNH₂ and An-NH₂ in Fig. 1f, 1i, 1g and 1k respectively) have been shown to form a stronger bond to CdSe NCs compared to the carboxylic acid - same with dithiocarbamate, thiol and dithioic acid or (An-NHCSSH, An-SH and An-CSSH in Fig. 1j, 1l and 1m respectively). While binding affinity is important, their experiments showed that the electronic coupling does not correlate with bonding strength. This is reflected in the photon upconversion quantum yields (QYs), where the best performing functional groups for the wurtzite CdSe NC donors to anthracene acceptors are phosphonic acid, imidazole and carboxylic acid, with QYs from 12.5-13.5%, showing no correlation with binding affinity.

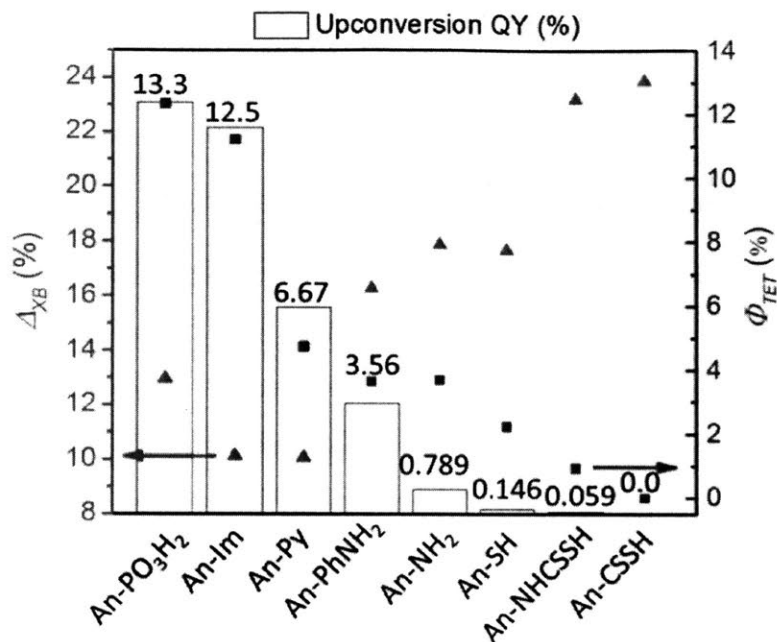


Figure 3-2: Plot of the photon upconversion QY for anthracene ligands (yellow bars), simultaneously shown with the relative decrease of initial exciton bleach of the CdSe NC donor (Δ_{XB} , red triangles, left), and the TET efficiency Φ_{TET} (blue squares, right).

3.1.2 Results

In the experimentalists' devices, the quantum dot absorbs a photon which rapidly interconverts to a triplet, the triplet then transfers to a tethered anthracene derivative, the tethered anthracene derivatives transfers the triplets to rubrene, where triplet fusion then occurs. So one hypothesis addressable by the quantum yields calculation of the sort done in chapter 2 is whether the lifetime of the triplet on the tethered anthracene is important. To that end, I have performed calculations to analyze whether the triplet lifetimes of the different ligands are responsible for the variations in upconversion quantum yield. To do this, I looked at the energetic cost of accessing the T1/ S0 minimum-energy crossing point, as well as the T1/S0 spin-orbit coupling constants. This analysis showed minimal variation between most of the molecules, with the exception of the dithiolate An-CSSH, for which the T1/ S0 minimum-energy crossing point is not much above the minimum (0.18 eV). An-CSSH and the other dithiolate An-NHCSSH also both possess spin-orbit coupling constants of over 100

	PO ₃ H ₂	Im	Py	PhNH ₂	NH ₂	SH	NHCSSH	CSSH
S0/S1 Gap at S0 Min (eV)	3.94	3.98	4.03	4.02	3.74	3.95	3.65	2.62
S0/T1 Gap at S0 Min (eV)	2.23	2.26	2.29	2.29	2.11	2.23	2.27	2.21
S0/S1 Gap at S1 Min (eV)	3.40	3.31	3.47	3.38	3.20	3.35	1.42	1.92
S0/T1 Gap at T1 Min (eV)	1.41	1.44	1.53	1.52	1.40	1.43	1.53	1.52
ΔG^\ddagger (for S0/T1 MECF (eV)	0.53	0.40	0.43	0.43	0.79	0.54	0.70	0.18
Largest S0 SOC at S0 Min (cm ⁻¹)	2.7 (T3)	2.2 (T2)	2.3 (T2)	2.3 (T2)	1.9 (T2)	25 (T5)	169 (T2)	203 (T1)
Largest S1 SOC at S0 Min (cm ⁻¹)	1.8 (T4)	2.4 (T4)	2.6 (T4)	2.6 (T5)	1.6 (T4)	15 (T8)	170 (T3)	148 (T3)

Table 3.1: TDDFT calculations were performed at the S0, T1, and S1 geometries, optimized on the DFT or TDDFT potential energy surfaces, respectively. These calculations were performed with the wB97x-D3 functional, a 6-31G* basis, and the Tamm-Dancoff approximation in the case of the TDDFT calculations. Calculations were performed with QChem 4.4

cm⁻¹. In addition, An-SH has a spin-orbit coupling constant of 6 cm⁻¹ which may also be sufficient to affect the efficiency of transfer from the ligand to DPA. The strong T1/S0 coupling leads to a short triplet lifetime and a low photoluminescence QY which impedes the TET from anthracene ligands to DPA (the upconversion annihilator). Therefore, even though the three sulfur-containing ligands have high binding affinities, they have low η TET and barely any upconversion.

For the four transmitter ligands with aromatic bridges, An-Im, An-Py, An-PhCOOH, and An-PhNH₂, other than the binding affinity, the coupling of T1 states to S1, S0 states affects the upconversion as well. A pyridine anchoring group routinely gives 1.8x higher photon upconversion QY than a benzoic acid or aniline bridge. Compared to benzene (phosphorescence QY, η P = 0.02546), η P of pyridine vapor is 1.5x10⁻⁵,⁴⁷ which is much lower than that for benzene. The lower η P of pyridine indicates a weaker coupling of T1 to S1 state and less reverse intersystem crossing which dissipates the triplet state of the transmitter. This explains that An-Py (upconversion QY 6.7 %) outperforms An-PhCOOH and An-PhNH₂ (upconversion QY 3.9% and 3.6% respectively) as a transmitter ligand when mediating TET between the CdSe donor and DPA acceptor. Additionally, the upconversion QY for An-Im is higher than An-Py, and An-PhNH₂. This is because of the short lifetime of An-Py and An-PhNH₂ due to their strong coupling between T1 and S0 states. We observe an interesting feature in An-Py and An-PhNH₂: a local minimum on the T1 surface near the CI (see Figure 5), which is absent in the other species. This local minimum

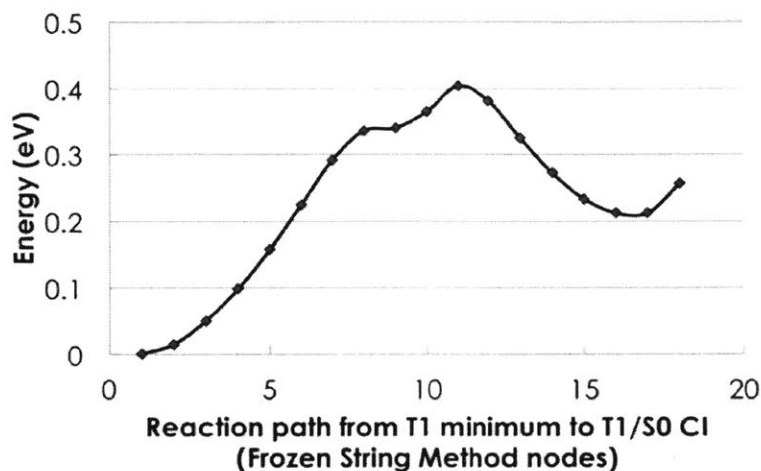


Figure 3-3: The energetics of the reaction path on the T1 surface of An-Py going from the T1 minimum-energy geometry to the T1/ S0 minimum-energy crossing point geometry, as computed using nodes and the freezing string method.⁴⁵ The first node is at the global minimum and the final node is at the intersection between the T1 and S0 potential energy surfaces. The lower-left structure displays the geometry of An-Py near the global minimum (node 1 on the reaction path above); the lower-right structure is of the local minimum near the minimum-energy crossing point (node 16 on the reaction path above) with the S0 surface, only 0.20 eV above the global minimum. This local minimum seems to be caused by steric clashing between the ortho hydrogens on the aryl groups and the hydrogens in the 1 and 8 positions on the anthracene. This local minimum on the T1 surface can confine the anthracene near a T1/S0 conical intersection, accelerating intersystem crossing between the two states and lowering the triplet lifetime.

is caused by steric clashes between the ortho hydrogens of the aryl side groups and the hydrogens in the 1 and 8 positions on the anthracenes. This can trap the ligand into a conformation from which the CI is both more accessible and more "peaked", a feature which is thought to speed up transfer through the CI. This helps explain why An-Py and An-PhNH₂ has a shorter triplet lifetime and lower upconversion QY than An-Im, despite their similar chemistries.

3.2 BODIPY Dyes

3.2.1 Introduction

We turned to boron dipyrromethene (BODIPY) dyes as our next family in large part due to their utility. They have applications as bio-sensors, photosensitizers for photodynamic therapy, laser dyes, waveguides, organic light-emitting diodes, and organic photovoltaic devices. An additional advantage of their breadth of use is the number of papers on them - it allows us to find papers with sufficient high-quality data, a surprisingly difficult task. So far, we have examined a series of chlorinated derivatives investigated in Duran-Sampedro, et. al. (see Figure 3-4).

One common idea in BODIPY dye studies is that adding a phenyl ring to the 8-carbon (as in species 1-10 in Figure 3-4) increases the non-radiative rates. A number of creative ideas for why this exists, the most prominent being a rather hand-wavey suggestion that the rotational mode of the phenyl couples the S₁ and S₀ states. Recently, studies have focused on a conformer in which the phenyl group is roughly co-planar with the BODIPY core. In this conformer, the energy gap is indeed smaller than before, but not by terribly much. What we have found is that there is an easily accessible conical intersection between the S₀ and S₁ surfaces near the co-planar conformer.

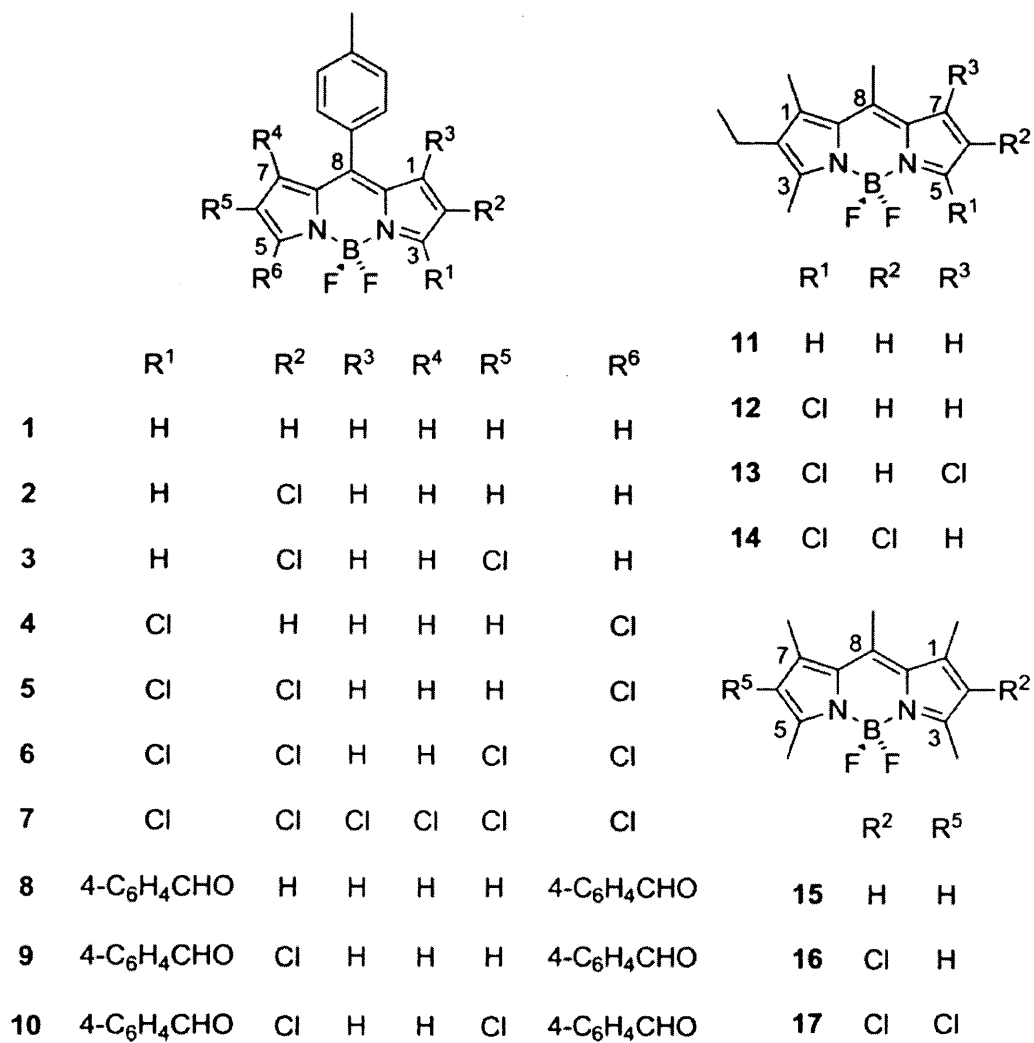


Figure 3-4: The set of BODIPY dyes investigated in Duran-Sampedro, et. al.

3.2.2 Preliminary Results

In Figure 3-5, I show the correlation between the experimental fluorescence energy versus the experimental non-radiative rates. The blue points are the species with a phenyl group. As mentioned in the section on naphthalene derivatives, an inverse energy gap law relationship is observed. This is characteristic non-radiative decay being limited by a conformational transformation, confirming previous studies. However, we can go further and say that there is a CI nearby. Figure 3-6 shows the reaction path of dye 1 from the Franck-Condon local minimum to the minimum energy conical intersection (as computed with SF-TDDFT/BHHLYP, the TDDFT results shown here do not quite agree but do show a very small gap). The transition state for this transformation occurs at the clash of the ortho-hydrogen on the phenyl group with the hydrogen on the 7-carbon (or the 1-carbon). This also suggests that a strong kinetic isotope effect could be observed here, as we would expect the quantum tunneling of the hydrogens past one other to be relevant.

The other seven species are more resistant to easy explanation. As can be seen in 3-5, they don't follow an inverse energy gap law. Although I have had some success finding a reaction path for dye 13, the number of conformational degrees of freedom caused by the extra methyl and ethyl groups makes convergence challenging. The rest of the dyes I leave to my successors.

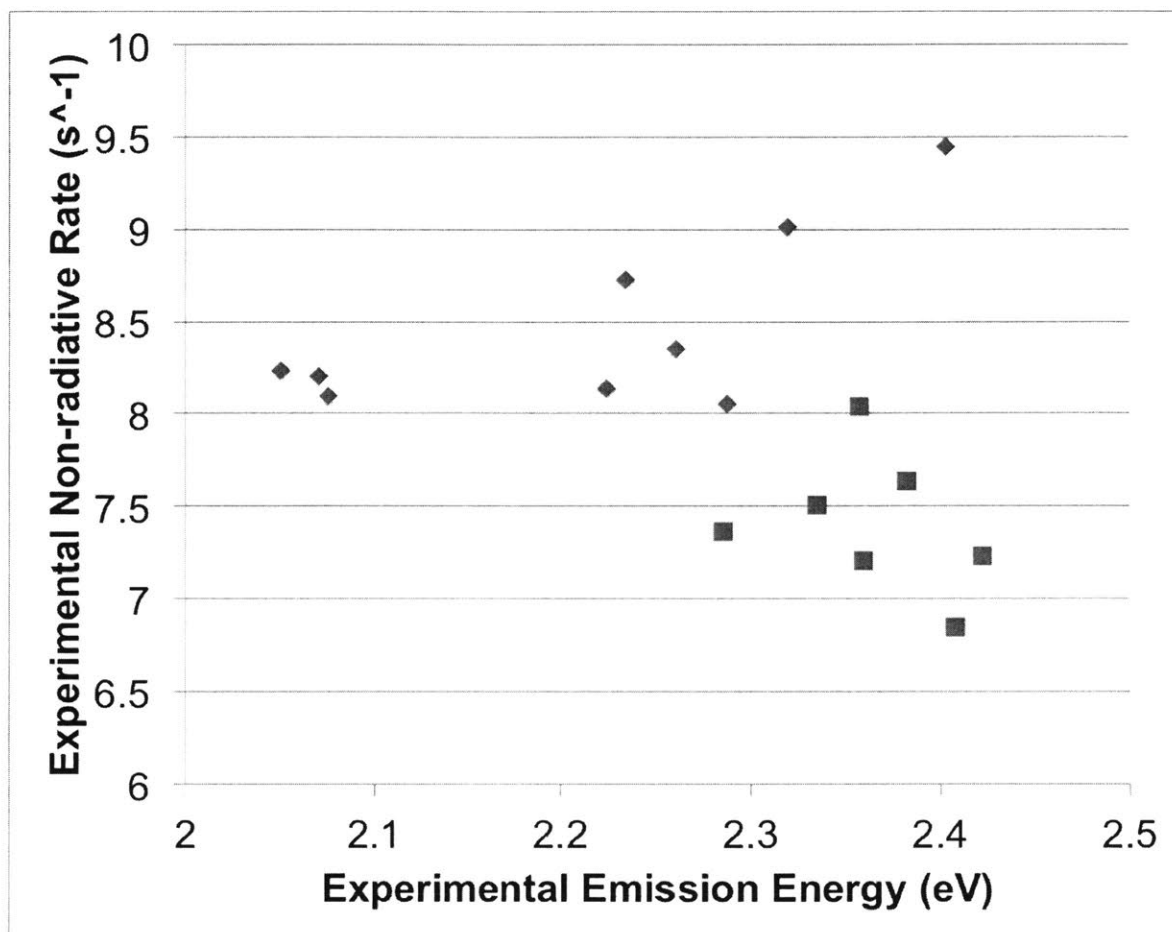


Figure 3-5: Plot of the experimental fluorescence energy versus the experimental non-radiative rates. The points in blue are species 1-10, bearing a phenyl group on the 8-carbon. The points in red are species 11-17, bearing a methyl group on the 8-carbon.

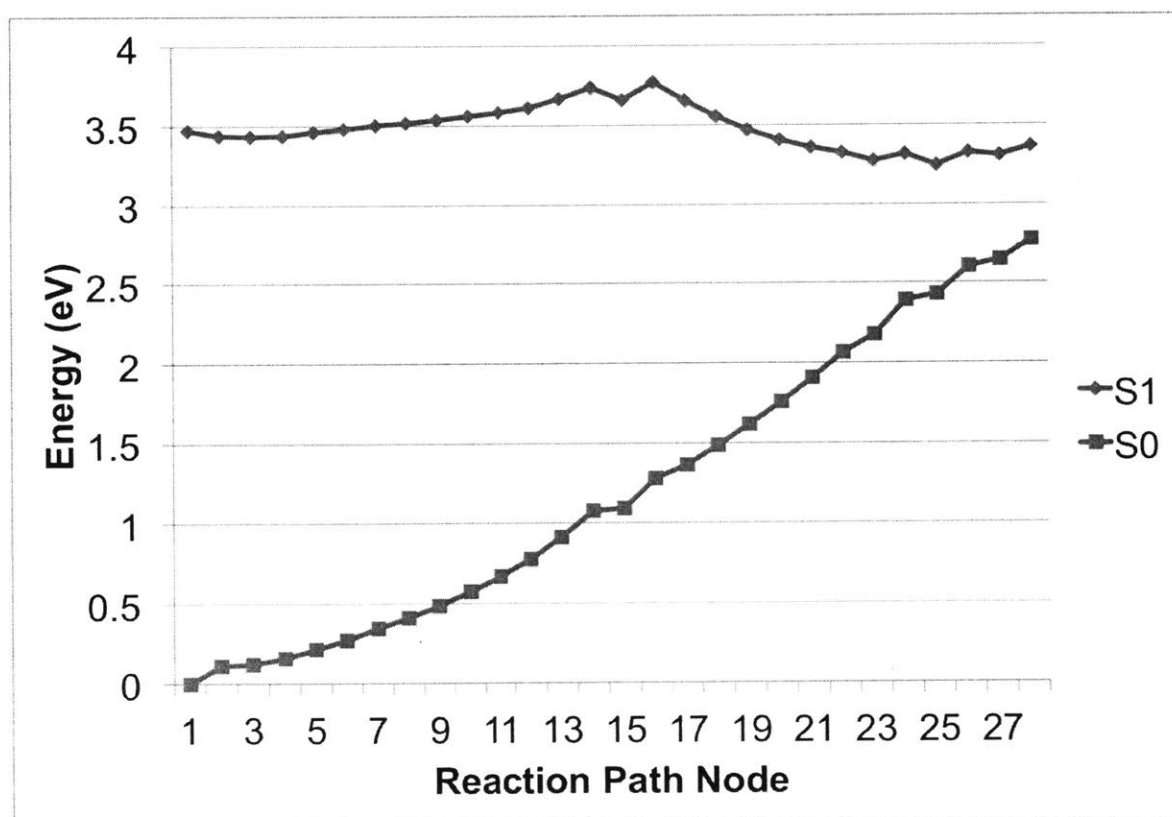


Figure 3-6: Plot of the reaction path of BODIPY dye 1, which has a phenyl group on the 8-carbon and no chlorination.

Chapter 4

Carrier Levels in Disordered Organic Photovoltaics: PPV and P3HT

4.1 Introduction

Photovoltaic materials show great promise in helping us overcome challenges in power generation, having played an increasingly important role in the energy market over the last decade [55, 56]. Organic photovoltaic (OPV) technology in particular has attracted research attention in the past few decades due to its superior tunability and higher theoretical efficiency compared to traditional silicon-based solar cells. In recent years, efficiencies in excess of 10% have been achieved [57, 58, 56]. However, improvement is necessary if OPVs are to compete with silicon [59]. To effect this improvement we need a better understanding of how OPVs operate on the molecular level.

In solar cells employing inorganic semiconductors, absorption of photons generates weakly-bound charge carriers due to the large dielectric constant of the medium [60]. However, OPVs have a much smaller dielectric constant, thus the electron and hole are coulombically bound together as they cannot be screened enough to separate - this forms an exciton. In order to generate charge carriers in these systems a driving force must be produced to separate the exciton. One common device structure, the bulk heterojunction (BHJ), induces separation using an interface between two

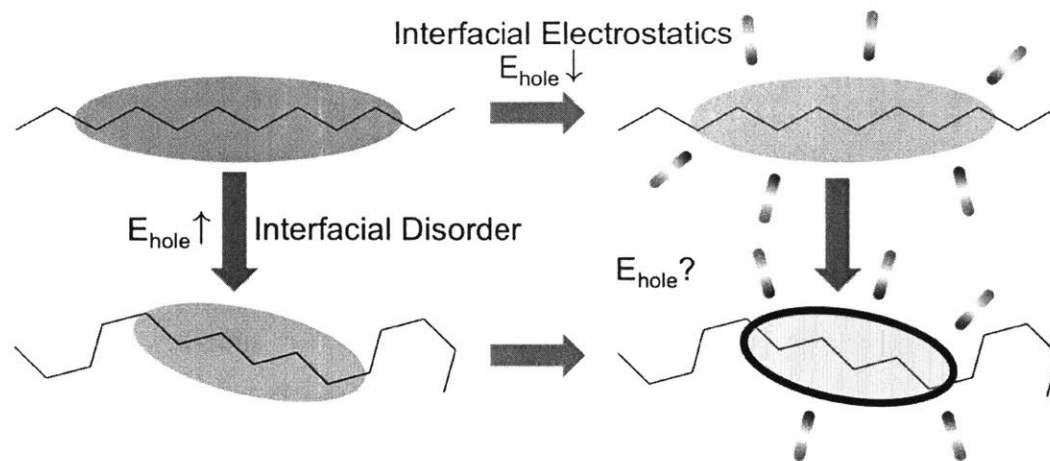


Figure 4-1: Schematic representing current state of studies on interfacial hole states in polymer-fullerene BHJ devices. The upper left diagram represents the hole state of an ordered polymer *in vacuo*. Some studies have investigated and elaborated on the role of the electronic environment near the interface (top right) [1, 2, 3]. Others have examined disorder of the polymer chain and how that impacts the energetics and spatial extent of the hole state (bottom left) [4, 5]. Herein, we examine both in a realistic system in order to evaluate how the two balance one another (bottom right).

different materials, usually a polymeric electron-donor phase that is thought to host most of the excitons and a fullerene-based electron-acceptor phase. [61]. Because exciton diffusion lengths in OPVs are short, it is necessary to have the interface near to where the excitons are generated [62, 63]. Due to this constraint, BHJs are constructed with the two domains interpenetrating one another in order to maximize the interfacial surface area and provide excitons with the shortest possible path for charge separation [64]. At the interface between the materials, the highest occupied molecular orbital of the donor and the lowest unoccupied molecular orbital of the acceptor have different energies[61]. This difference drives the exciton to separate into charges and determines the open circuit voltage of the OPV device [65]. Simple calculations of the binding energy of the charge-transfer (CT) state at the interface suggest that charge separation requires around 0.2 - 0.3 eV, a prohibitively high barrier at room temperature [66]. Despite this problem, experiments show near-unity interfacial charge separation efficiencies in many OPVs [67, 68, 69].

We wish to address here the mystery over why charges separate at interfaces,

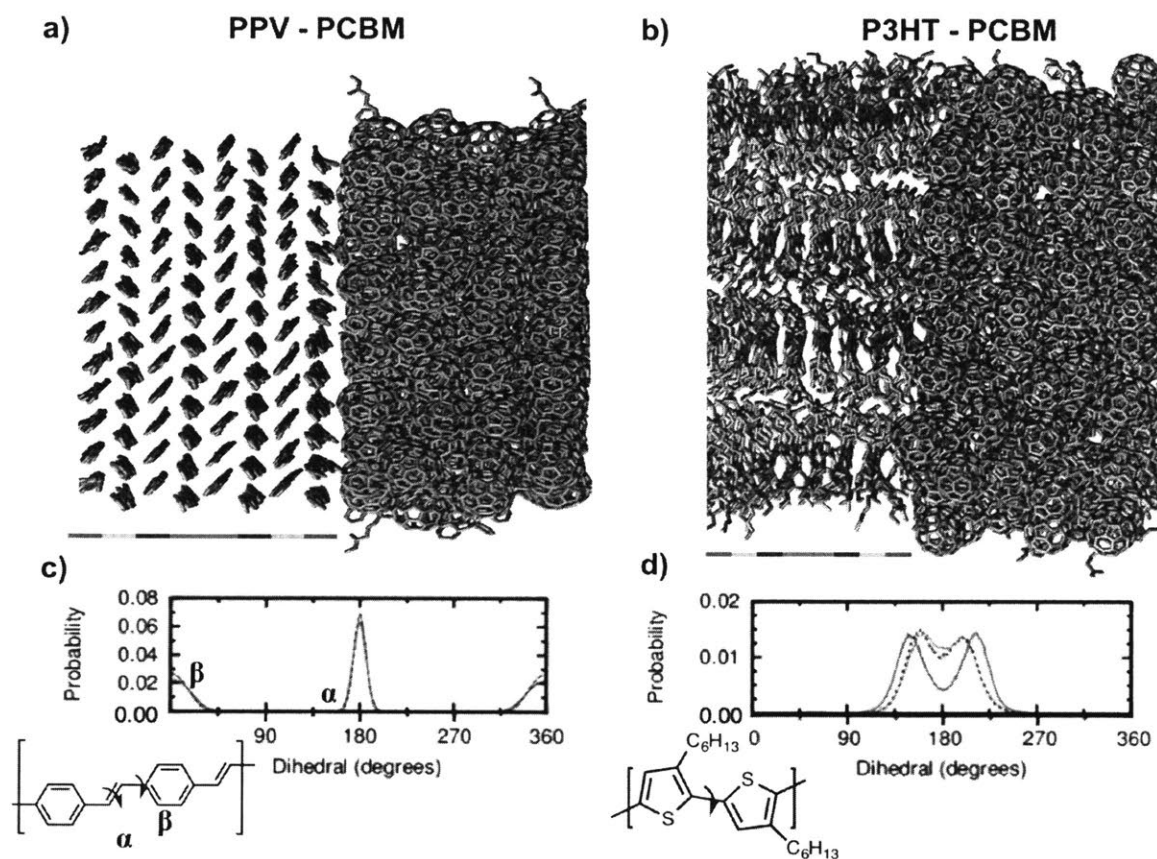


Figure 4-2: Images of the interfaces of (a) PPV/PCBM and (b) P3H PCBM and their dihedral angle distributions, (c) and (d) respectively. The dihedral angle distributions are separated based on their distance from the PCBM interface - red for the closest layers, purple for the farthest.

which has generated controversy in the field. Some have suggested that this may be explained by invoking 'hot' high-energy CT states, in which excess energy from the charge-transfer process is used to overcome the charge binding energy [70, 71, 72]. *Ab initio* calculations testing this hypothesis show that an electronically and vibrationally excited 'hot' CT state can indeed undergo facile interfacial charge separation [73, 74]. However, to date there is mixed experimental evidence for the necessity of 'hot' states. There is evidence that a larger donor-acceptor offset is correlated with more efficient charge separation [75, 76, 72], suggesting that the energy released by the charge transfer event effects charge separation. Recent work has shown that one can directly probe optically-accessible CT states and found that for these states, the charge separation efficiency is independent of excitation energy [77, 78, 79, 80, 3]. That is, 'hot' CT states and 'cold' CT states are equally efficient at dissociating. Others have criticized this interpretation, pointing out that these optically-excited CT states have not fully relaxed and that this polaronic stabilization energy is substantial [81].

Generally speaking, there are two broad theoretical explanations for the apparent 'cold' CT state separation. The first posits that the electrostatic properties of the interface cause the band structures of the donor and acceptor molecules to bend such that there exists an energetic gradient that separates the charges. Various mechanisms have been suggested: the dielectric mismatch of the organic semiconductors [2, 3]; poor packing of molecules near the interface[4, 5]; and the presence of a static electric field near the interface [1].

The second explanation focuses on the role of delocalization of the charges in the charge-separated state [3, 82, 83]. Due to the polymeric nature of the donor, the hole state can delocalize quite easily, decreasing its coulombic interaction with the electron and reducing the hole-electron binding energy [4, 66, 2]. Other studies have implicated delocalization of the electron across multiple fullerene units in the acceptor phase [81, 84, 85].

To understand the band structure near the interface, it is desirable to perform electronic structure calculations on representative systems. Unfortunately, BHJs are

very disordered near the interface, and the exact nature of this disorder has a large impact on the performance of the device [86, 87]. Because of this, it is necessary to sample an ensemble of physically realistic states, mandating the use of molecular dynamics (MD). Previous studies have used MD to generate states for simulating the band structure of P3HT, but have not examined the combined effects of disorder and electronic polarization [88, 89].

Herein, we build on previous work suggesting that electronic polarization effects are important by incorporating Drude particles into our MD simulation and analyzing their impact on the interfacial electronic states [90, 91, 5]. Our simulations include both realistic disorder in the molecular structures and the impact of the variable electrostatic environment near the interface, as summarized in Figure 4-1. We find that these polarization effects are necessary to reproduce the experimental band gap for the bulk species and have a substantial effect on the band structure near the interface. To probe the effect of disorder on charge carrier delocalization and band gaps, we examine interfaces with a relatively crystalline donor phase (poly(*p*-phenylene vinylene, PPV) and a relatively amorphous donor phase (poly(3-hexylthiophene-2,5-diyl), P3HT). We find that in PPV there is indeed little interfacial disorder, and that the interfacial band structure is dominated by a static electric field generated upon the inclusion of polarization effects. P3HT shows interfacial disorder-induced localization that promotes charge separation, but the effect is overpowered once electronic polarization effects are included. Taken together, these results imply that electronic polarization should take precedence over polymeric ordering when rationally designing the interfacial band structure of BHJ devices.

4.2 Computational Details

We examine two systems here: the PPV/ [6,6]-phenyl-C₆1-butyric acid methyl ester (PCBM) interface and the P3HT/PCBM interface. These two interfaces were chosen because PPV and P3HT are both well-characterized experimentally and show contrasting degrees of crystallinity [92, 93], thus allowing us to probe the effect of

molecular ordering on the band structure [94]. There is some controversy in the literature regarding how crystallinity impacts BHJ efficiency, as there seems to be a tradeoff where increased crystallinity improves charge mobilities but decreases interfacial charge separation [95, 96, 97, 98, 99, 100]. We wish to address some of the ways that increased crystallinity may affect charge separation here.

The interfaces we model here are not perfect representations of the interfaces that appear in devices. Our simulations employ sharp interfaces between the donor and acceptor phases. However, under some processing conditions miscibility between the donor and acceptor phases is observed and an amorphous mixed phase seems to be present [101]. Another difference is that the PPV we simulate lacks side chains, whereas experimentalists commonly use PPV derivatized bulky side chains that substantially impact crystallinity and interfacial structure [102]. Use of our data to understand in situ experimental interfaces should bear these caveats in mind.

4.2.1 Molecular Dynamics

The PPV-PCBM interface employed a crystalline slab of 96 PPV molecules abutting 240 PCBM molecules. Each PPV oligomer contained 14 monomer units, with the crystalline phase arranged into 8 layers of 12 chains. The starting PPV configuration was taken from an experimental crystal structure [103] and the force field was adapted from the work of DuBay and coworkers [104], with point-charges taken from the central monomer of a B3LYP/6-31G** CHELPG calculation on a trimer.

The P3HT-PCBM interface simulations were performed with 32 P3HT molecules and 240 PCBM molecules (see Figure 4-2). For P3HT, the crystalline phase was composed of 20-mer chains organized into 4 layers, each consisting of 8 chains each, with the starting configuration developed as in reference [4]. We chose this polymer length because the hole polaron in P3HT is thought to be delocalized over approximately 15 monomer units, allowing us to minimize the finite size effect on the energies [105]. The majority of the force-field terms for P3HT are taken from previous studies [106, 107], with the non-bonded terms (e.g., van der Waals terms) for all three systems (PPV, P3HT, and PCBM) coming from an optimized potentials for liquid

simulations (OPLS) all-atom force field [108].

The starting PCBM configuration came from an experimental crystal structure[109] and consisted of 240 molecules. The force field was derived from previous studies [110, 111].

The initial P3HT, PPV and PCBM systems were equilibrated (with independent PCBM simulations run that had interfacial surface areas equal to each of the polymer systems). Configurations were first energy minimized, followed by a 1 ns NVT simulation at 100 K, then with a 1 ns NPT simulation at 100 K and 300 K using a 1 fs timestep, 12 Angstrom cutoff with a potential shift for Lennard-Jones and short-range Coulombic interactions, the Berendsen thermostat, particle mesh Ewald for the long-range electrostatics, and an anisotropic barostat with relaxation times of 0.1 and 1.0 ps, respectively. The equilibrated systems were resized to have equal surface area and aligned adjacent to one another with a 3-4 Angstrom gap between them. An energy minimization was then performed to remove close contacts, followed by a 1 ns NVT run at 500 K in which the P3HT was held rigid and the PCBM allowed to move to wet the interface. This was followed by a 1 ns NPT run at 100 K, and finally a 5 ns NPT run at 300 K, the last 2 ns of which were used for subsequent analysis. Snapshots from these runs were taken every 40 ps in order to decrease the correlation between snapshots. All molecular dynamics simulations utilized Gromacs [112]. Short-range interactions used a All system visualizations were performed with VMD [113]. Forcefield parameters and the coordinates of a representative snapshot can be found in the Supporting Information (SI).

4.2.2 Electronic Structure Calculations

From a given MD snapshot, multiple molecules are chosen and separate quantum chemical calculations are performed on each one. We performed the calculations while treating the molecular environment in three ways: as absent (*i.e.*, in vacuum); as point charges; or as point charges with corresponding Drude particles. Calculations *in vacuo* for these systems that incorporate atomistic disorder have been performed elsewhere in the literature (*e.g.*, in work by Troisi[4]). However, treatments of the

Table 4.1: Calculated transport properties for PCBM, PPV, and PCBM. The ionization potential (IP) and electron affinity (EA) have been calculated for the bulk phase of the three materials and with the three environmental treatments being considered. The transition gap (TG) is computed as $E_{\text{IP}} - E_{\text{EA}}$. Improved treatment of the environment brings theoretical values in line with experimental values. Each value has a standard deviation of 0.05 eV.

		IP (eV)	EA (eV)	TG (eV)
PCBM [75] ($\epsilon = 3.9$)	Vacuum	7.45	1.74	5.71
	Static	6.92	2.23	4.69
	Polarizable	6.25	3.43	2.82
	Experimental	5.9-6.1	3.7	2.4
PPV [118] ($\epsilon = 2.6$)	Vacuum	5.73	1.75	3.98
	Static	5.51	1.85	3.66
	Polarizable	5.28	2.28	3.00
	Experimental	4.9	2.8	2.1
P3HT [75] ($\epsilon = 3.4$)	Vacuum	5.35	1.31	4.04
	Static	5.12	1.25	3.87
	Polarizable	4.91	2.11	2.79
	Experimental	4.8	2.2	2.6

electrostatic environment have not been. Drude particles are useful in this context because they simulate electronic polarizability, whereas a point charge treatment alone does not respond dynamically to the electronic field of the interrogated molecule. We shall refer to these three levels of treating the environment as "Vacuum", "Static", and "Polarizable".

The Drude particles' locations in the chemical system are described in the supporting information (SI) and their parameters were optimized to reproduce the experimental dielectric constant. All quantum chemical calculations were performed at the LRC-wPBEh/6-31g* level [114] using QChem (version 4.1) [115]. This functional was chosen as it has been shown to describe the extent of delocalization in polymer chains well [116, 117] and employs 20% Hartree-Fock exchange and $\omega = 0.2 \text{ bohr}^{-1}$.

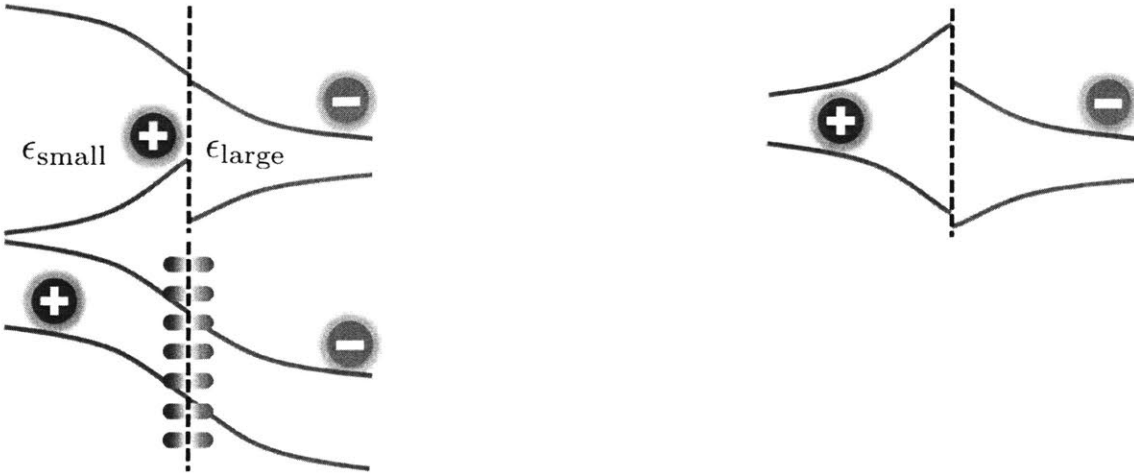


Figure 4-3: The impact of different interfacial contexts on the band structures. A dielectric mismatch in which the acceptor phase has a larger dielectric than the donor phase (left) causes the bands of the donor phase to become stabilized and the bands of the acceptor phase to become destabilized as the hole and electron become better and worse solvated, respectively. Interfacial disorder (center) disrupts conjugation, confining and destabilizing the hole and electron states. A static interfacial electric field (right) stabilizes the electrons and destabilizes the holes in one domain (depicted here as the donor phase), and destabilizes the electrons and stabilizes the holes in the other.

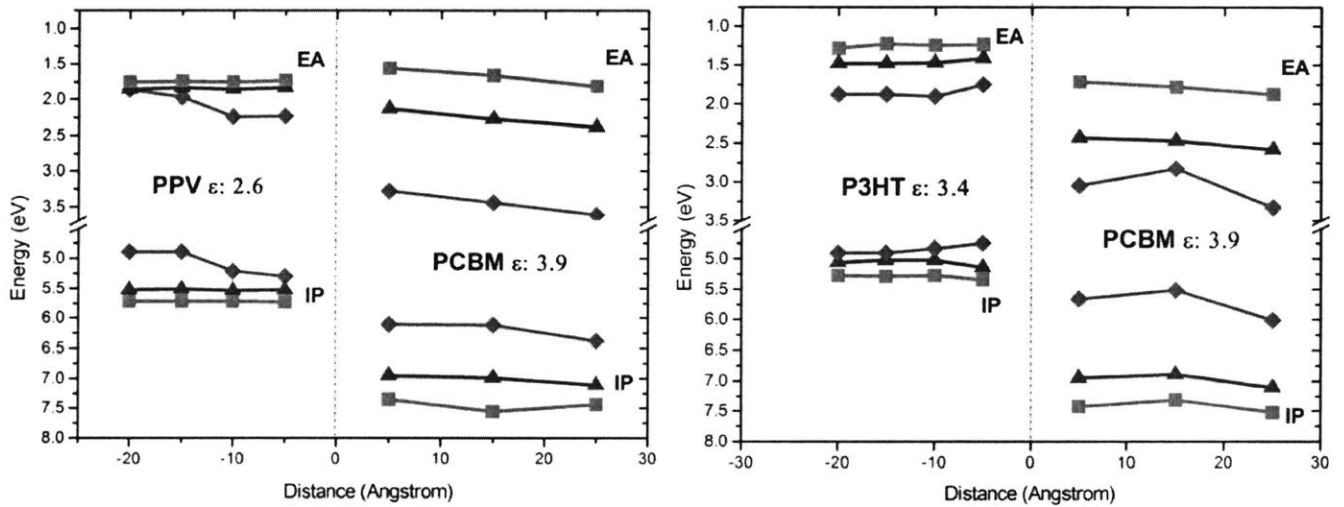


Figure 4-4: The band structures at the PPV-PCBM interface (left) and the P3HT-PCBM interface (right) with differing treatments of the environment: as vacuum (red); static point charges (blue); or as static point charges with Drude particles (green). In both systems, inclusion of polarization effects dramatically changes the band structure. Each point has been averaged from 102 calculations and has a standard deviation of 0.05 eV. The distances are resolved by binning each molecule into a layer and using the average distance from the interface of that layer.

4.3 Results and Discussion

Bulk Properties

We parameterized the Drude particles to reproduce the bulk polarizabilities of PPV, P3HT, and PPV, as computed from the Clausius-Mossotti relation and the experimental dielectric constants. During this procedure, we calculated the bulk ionization potential (IP), electron affinity (EA), and transport gap (TG, $E_{IP} - E_{EA}$) for each organic semiconductor. These results are reported in Table 4.1.

For all three bulk systems, inclusion of environmental polarizability drastically improves the agreement of these quantities with their experimental values. For PCBM, Drude particles stabilize both charged states by around 0.7-0.8 eV, consistent with the Born model solvation energy for a charge in a spherical cavity of radius 7 Angstroms and continuum dielectric of 3.9 (0.76 eV) [119, 5]. The two polymers display a similar behavior, but of a lesser magnitude. For PPV and P3HT, the ionized states stabilize by only 0.3 eV and 0.4 eV respectively. Even accounting for the polymeric systems' smaller dielectric constants, a Born model calculation would imply an unphysical cavity radius of tens of Angstroms. This suggests more forces are relevant than simply electrostatics - namely, a delocalization pressure. That is, as the dielectric increases, the size of the polaronic charge will tend to contract so as to maximize the interaction with the dielectric. This contraction will increase the kinetic energy of the hole, reducing the apparent stabilization energy. We can probe this interplay by modeling the electrons and holes as particles in a one-dimensional box solvated by the spherical born model:

$$E = - \left(1 - \frac{1}{\epsilon} \right) \frac{1}{L} + \frac{\pi^2}{2\mu L^2} \quad (4.1)$$

where ϵ is the relative dielectric of the medium, L is the diameter of the box, and μ is the effective mass of the pseudoparticle (which accounts in an approximate way for the deviation of the true potential from a particle in a box). At the equilibrium value of L (30 Angstroms for $\epsilon \cong 4$), this expression reduces to:

$$E|_{\frac{dE}{dL}=0} = -\frac{\mu}{2\pi} \left(1 - \frac{1}{\epsilon}\right) \approx -1.38 \mu \left(1 - \frac{1}{\epsilon}\right) \text{ eV} \quad (4.2)$$

Typical effective mass values for holes and electrons in organic polymers are around $0.2 m_e$ [120]. When we evaluate the solvation energy by subtracting the energy of the unsolvated charge (with $L = 37$ Angstroms), we find stabilization energies for PPV and P3HT of 0.18 eV and 0.21 eV (these numbers are sensitive to the exact value of μ used). These values are much closer to the numbers we computed, showing that this simple model can explain the lower stabilization energies.

Interfacial Molecular Structure

The constructed interfaces show starkly different levels of structural disorder, as can be seen visually in Figures 2a and 2b. In PPV the torsional angles have very tight distributions (Fig. 4-2, part c), a feature which varies minimally as we approach the interface. This contrasts dramatically with the situation for P3HT (Fig. 4-2, part d), where we observe a broad dihedral distribution that separates significantly as we approach the interface. These results confirm what can be seen by visual inspection of the two interfaces: the P3HT/PCBM interface is more disordered than the PPV/P3HT interface. Additionally, these findings agree well with experimental studies of these systems [94] wherein PPV is known to be much more structured than P3HT and reflects our use of PPV and P3HT as generic models of an inflexible and flexible donor, respectively.

Interfacial Electronic Structure

We evaluated the IP/EA levels of molecules as a function of distance from the interface in order to determine how the interface affects the energetics of charge separation (Fig. 4-4). Figure 4-3 shows how common interfacial phenomena impact the local band structure [5]: a dielectric mismatch promotes the separation of one of the charged species to the bulk, interfacial disorder disrupts conjugation, confining and destabilizing the charge carriers, and a static interfacial electric field either works

with or against separation for both charge carriers.

Turning to the PPV-PCBM interface (Fig. 4-4, left), we observe that the IP and EA levels of the polymeric donor phase are agnostic towards the interface unless we include electronic polarization effects. This suggests both that the high degree of crystallinity of PPV persists at the interface and that the static charge distribution of interfacial PCBM molecules has little impact, hence, the hole levels do not change as we approach PCBM. When we include electronic polarization effects, charge carriers in PPV display contrasting responses to the interface, with interfacial electrons becoming stabilized and interfacial holes relatively destabilized. This asymmetric interfacial shift (where the EA and IP levels both go down) implies that an electric field may be induced at the interface that is preferentially stabilizing the electron levels. We expected the dielectric mismatch between PPV ($\epsilon = 2.6$) and PCBM ($\epsilon = 3.9$) to stabilize the interfacial holes, but that effect appears to be negligible in our calculations. Because holes flow "uphill" (towards regions with lower IP), the topology of this band structure encourages charge separation. The PCBM bands in the PPV-PCBM interface appear to show some influence from the dielectric mismatch, with the band gap broadening slightly, and a larger effect from the inclusion of polarization bending both levels up.

For the P3HT-PCBM interface (Fig. 4-4, right), the levels without polarization effects show a broadening of the interfacial band gap consistent with a disordered interface. This disorder disrupts conjugation, raising the confinement energy - this lowers the interfacial EA and raises the interfacial IP, thereby providing an energetic pressure for charge separation. When electronic polarization effects are enabled, however, interfacial P3HT hole states are stabilized (the IP band bends upward), which could be explained by the higher dielectric of the acceptor phase (although the electron levels in P3HT are mostly unaffected, perhaps due to being localized on a different part of the polymer with a different electrostatic environment). The PCBM domain shows surprisingly non-monotonic behavior in its band levels that resists an easy explanation. Despite this, the transport gap is decreasing monotonically as we look at PCBM molecules farther away from the interface, a result that is well-explained by

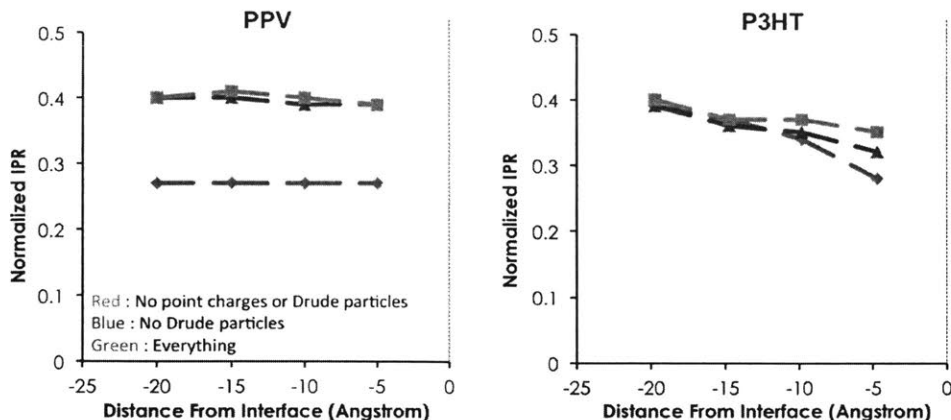


Figure 4-5: The normalized inverse participation ratios (NIPR) for the holes states in the electron-donating polymers being considered, PPV and P3HT. The NIPR was computed for each system with the environment treated as vacuum (red); static point charges (blue); and as static point charges with Drude particles (green). In PPV (left), the extent of delocalization of the hole states shows little influence from the interface, irregardless of the environmental treatment. In P3HT (right), the hole states are more localized near the interface than the bulk, with this effect strengthening as the environment is treated with greater sophistication. Each point has been averaged from 102 calculations and has a standard deviation of 0.01. The distances are resolved by binning each molecule into a layer and using the average distance from the interface of that layer.

the lower dielectric of P3HT.

Reflecting on the competing influences of electrostatic environment and molecular disorder in determining the interfacial band structure, we observe in PPV that the interfacial disorder seems to have no effect on the energy levels of PPV, but that electronic polarization effects do create a significant pressure for charge separation. In contrast, P3HT shows the impact of disorder on the hole energies, as the gas phase calculations show a significant decrease of the hole energy levels near the interface, promoting charge separation. Nonetheless, this effect is washed out by inclusion of the electrostatic environment - in both systems environmental electrostatics dominate the interfacial band structure in a manner that promotes charge separation.

Hole Delocalization

In this study we are also interested in examining how the interface affects delocalization in the hole electronic states. One common method of doing this is by looking

at the HOMO of the neutral polymer species [2, 121, 122]. However, this measure neglects orbital relaxation, causing the hole to appear over-delocalized. Herein, we employ the normalized inverse participation ratio (NIPR), which counts the effective fraction of the polymer a hole state is spread over. We compute this as:

$$\text{NIPR} = \frac{1}{N} \frac{1}{\sum_{i \in \text{Sites}} \frac{1}{P_i}} \quad (4.3)$$

Where P_i is the population on each site of the hole state, which in this case is taken as the charge on each monomer within the polymer. This per-monomer population is computed as the difference in the Mulliken populations for the cationic and neutral forms of the polymer. The NIPR ranges between two extremes. For a model polymer in which the hole is equally distributed over N sites, each with population $\frac{1}{N}$, $\text{NIPR}=1$, the hole is distributed over the entire polymer. For a polymer in which the hole is entirely localized on 1 site, $\text{NIPR}=\frac{1}{N}$, reflecting the fact that the hole occupies only a small part of the polymer.

We compute the NIPR in the per-monomer basis instead of the per-atom basis because the per-atom basis results in sites with negative populations due to inductive effects and instabilities in the construction of Mulliken charges. The per-monomer treatment taken here has no negative-population sites, assuring us that the Mulliken populations used are reasonably accurate.

The average NIPR values for the hole states per layer are shown in Figure 4-5. NIPR data for the electron states in the polymers is in the SI.

As anticipated, PPV shows little sensitivity to the interface - the NIPR does not change as we approach the interface. The P3HT analysis shows a very different situation. Hole states in P3HT that are nearer to the interface are more localized. This arises from interfacially-induced disorder that causes a form of Anderson localization and has been observed in theoretical studies on P3HT *in vacuo* [93, 123].

As we compare different levels of environmental electrostatics, some interesting results accrue. For PPV, adding static point charges has a negligible effect - the NIPR remains constant and shows that the hole is localized on around 40% of the

polymer. Drude particles dramatically localize the hole state to around two-thirds of the prior extent. In contrast, P3HT shows a change of a much smaller magnitude. Improved treatment of the electronic environment increases the degree of interfacial localization, but at most this only reduces the hole size around 20%. The starkly different responses of these two materials to Drude particles suggests that the hole delocalization of disordered materials may be well-described without resorting to use of a polarizable environment, but this result may not be general.

These results are in concordance with our earlier interpretation of the band diagrams in Figure 4-4. PPV shows little structural impact from the interface, with the hole being equally delocalized near the interface and far away. There is, however, a significant dielectric confinement effect, wherein the $\frac{1}{L}$ dependence on the Born solvation energy squeezes the hole, increasing its kinetic energy. As inferred above, P3HT's conjugation is disrupted near the interface, causing the observed destabilization of interfacial holes in the gas phase calculations. Although dielectric confinement effects increase the magnitude of the interfacial localization as observed in Figure 4-5, the expected destabilization of interfacial holes does not appear in the band structure, as the impact of this structural disorder on the holes is washed out by the improved dielectric solvation of the PCBM domain.

4.4 Conclusion

In this study we analyze the impact of electrostatic effects and realistic disorder in simulations of BHJ interfaces. As we treat the environment with more sophistication, we observe that the band structure near the interface changes. The band gap narrows considerably for all molecules under consideration and substantial dependence on the interfacial distance develops due to interactions with a physically-realistic polarizable environment. For PPV, the interface causes little disorder, so that the final interfacial band shape emerges entirely from environmental electrostatics and shows a substantial pressure for charge separation. In P3HT, the interfacial chains are more disordered, localizing the hole states and raising their energies. The impact on the band structure,

however, disappears when we account for the environment.

With regards to the controversy over whether electrostatic or delocalization effects are primary in understanding charge separation, what we observe herein suggests that interfacial disorder can indeed significantly lower the extent of the hole wavefunction. This effect is augmented by the inclusion of a sophisticated environment, but the environment itself also has an effect on the interfacial band structure that goes in the opposite direction of, and typically is stronger than, interfacial localization.

When one considers OPV device design, there are many competing heuristics to balance. The results here suggest that one should give precedence to electrostatic environment considerations over interfacial disorder considerations when optimizing BHJ performance. Indeed, recent experimental devices incorporating a high-dielectric dopant into BHJs have found that despite this dopant introducing disorder into the system, the dielectric effect dominates and can be used to improve efficiencies [124].

Future work dedicated to understanding how these effects manifest themselves in novel high-efficiency BHJ devices such as PTB7-PCBM would be of value [125]. Additionally, much of the discussion on using charge delocalization to understand CT state separation is focused on delocalization in the acceptor domain between multiple fullerenes [73, 81]. Given our access to a realistically-disordered fullerene phase with a polarizable environment, such an investigation would be quite feasible. Finally, the systems we investigate here are still very ordered, with both the donor and acceptor phases merely perturbed from their crystalline geometries. A more realistically disordered system is less amenable to analysis, but would more completely describe the disorder found in real systems.

4.5 Supporting Information

Details on the construction of the Drude models, the IPR values, density of states plots, and forcefield parameters.

4.6 Acknowledgements

This work was funded by ENI S.p.A. as part of the MIT Energy Initiative. We thank Nadav Geva, Dr. James Shepherd, and Dr. Michael Mavros for helpful discussions.

Chapter 5

Carrier Levels in Disordered Organic Photovoltaics: PTB7

5.1 Introduction

Organic solar cells are a promising avenue of research in renewable electricity, forecasted to make up XX % of electricity generation in YYYY []. Due to their relatively low dielectrics, organic materials do not readily dissociate excitons into charge carriers. To generate charge carriers, organic solar cells are composed of two materials with different band levels. This difference drives charge separation at the interface between the two materials, with the "acceptor" phase receiving the electron from the "donor" phase. To maximize interfacial surface area, the two phases are engineered to intermix and form bicontinuous networks that allow the charges to reach their respective electrodes, a structure known as a bulk heterojunction (BHJ).

An outstanding question in the field is the mechanism by which the interface generates free charge carriers. Simple calculations of the interfacial charge-transfer (CT) state's binding energy suggest that separating the electron from the hole requires 0.2-0.3 eV, many times greater than kT . However, despite this barrier charge separation of efficiencies near-unity have been reported. How are charges dissociating so easily?

One solution to the quandary of interfacial charge separation is to invoke excess energy left over from the exciton, the so-called "hot" CT state hypothesis. How-

ever, recent experimental evidence increasingly suggests that interfacial sub-bandgap states, which are presumably "cold", also generate free charge carriers. The mechanism for cold CT state separation therefore remains a pressing question.

Past studies have suggested that the interface structure may promote charge separation through structural disorder or electrostatic effects []. Due to the disordered nature of BHJs, the interfacial structure is complex and difficult to study experimentally, demanding theoretical assistance. Our past research has focused on these how these interfacial features can impact the band levels, creating an energetic drive for or against charge separation. Herein, we examine the interface between a recent high-efficiency low-bandgap donor compound, polythieno[3,4-b]-thiophene/benzodithiophene (PTB7), and the most commonly used donor phase, [6,6]-phenyl-C61-butyric acid methyl ester (PCBM). PTB7 has record-high efficiencies of XXX%, which invites the question of whether the interfacial structure is important for that achievement.

We find that PTB7, as a highly disordered polymer intrinsically, experiences templated ordering near the interface. This templating, generally speaking, stabilizes near-interface electrons and destabilizes near-interface holes. With the inclusion of environmental electrostatic effects, the hole shows seems to experience more interfacial localization, while the electron experiences less. This asymmetric response may be a result of PTB7's internal structure as a "push-pull" polymer (see Figure 5-1), where different parts of the polymer are more electron-rich and electron-poor, presumably localizing the hole and electron differently.

5.2 Computational Details

Recent research in the BHJ field has focused on the observation that the two phases are partially miscible and that devices often have a partially intermixed region at the interface, as opposed to the sharp interface we have here []. However, this mixed region seems to negatively impact device efficiencies, and is controllable by optimizing the processing conditions []. For that reason, our focus here on a clean interface is

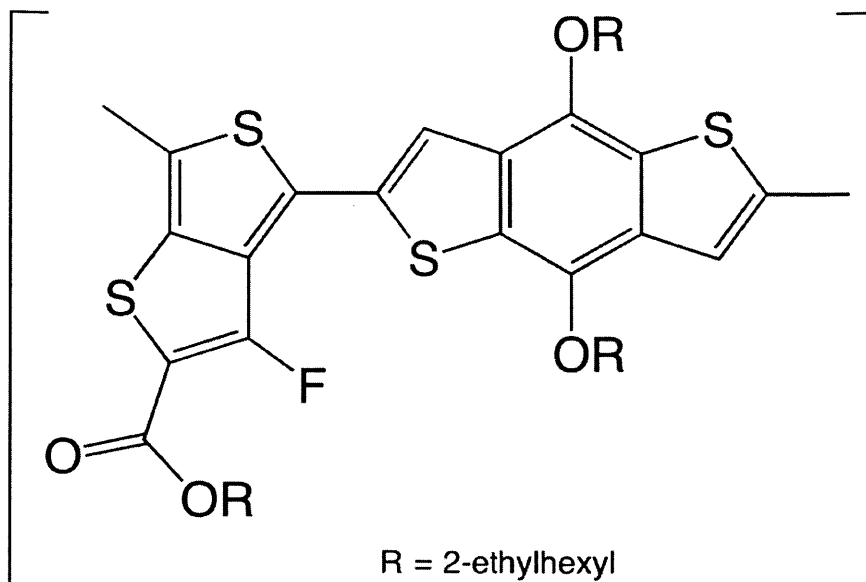


Figure 5-1: The base repeating unit in PTB7. The moiety on the left is relatively electron-poor, whereas the moiety on the right is relatively electron-rich.

both convenient (easier to define) and represents a sort of idealized interface that device engineers are striving for.

5.2.1 Molecular Dynamics

Our PTB7-BCM interface is composed of 24 PTB7 molecules and 204 PCBM molecules. Each PTB7 oligomer consisted of 6 monomeric units and the bulk phase was organized into 4 layers of 6 PTB7 chains. Only 6 units were needed as the monomeric unit is very large, meaning that experiments typically use around 6-unit oligomers. Additionally, the hole generally only delocalizes across 3-4 units. The force field we used was derived from an optimized potentials for liquid 176 simulations (OPLS) all-atom force field.

Our initial PCBM configuration came from an experimental crystal structure and consisted of 204 molecules. The force field was the same as we have used in previous studies.

We constructed the initial interface by placing the two bulk domains as near each other as possible while avoiding clashes with the PTB7 facing the PCBM molecules face-on. Initially, we performed an energy minimization. We then ran an NPT

simulation for 0.2 ns at 500 K and 1000 atm, followed by an NPT for 0.5 ns at 500 K and 5000 atm, followed by another energy minimization, followed by 1 ns of NPT at 500 K and 1 atm, followed by 1 ns of NPT at 100 K and 1 atm, followed by a 5 ns NVT at 300 K, followed by 1 ns of NPT at 300 K and 1 atm. We then performed a 5 ns NVT production run at 300 K, with snapshots taken every 50 ps from 1 ns on in order to avoid snapshot-snapshot correlations. Simulations were run with a 1 fs timestep, 12 Angstrom cutoff with a potential shift for Lennard-Jones and short-range Coulombic interactions, the Berendsen thermostat, particle mesh Ewald for the long-range electrostatics, and an anisotropic barostat with relaxation times of 0.1 and 1.0 ps, respectively.

All molecular dynamics simulations were performed using GROMACS []. Visualization of systems was performed using VMD [].

5.2.2 Electronic Structure Calculations

From a given snapshot, electronic structure calculations were run on every molecule in the system. Calculations were performed at different levels of environmental detail in order to tease out different effects: with the surrounding molecules absent (gas) and with the surrounding molecules treated as the ensemble of their atomic charges used in the force field (point charge). Looking at both of these contexts allows us to distinguish different effects from their impacts on the band levels.

Calculations were performed at the LRC-wPBEh/6-31G* level using the QChem 5.0.0 software package. This functional was chosen because it has been shown to reproduce the extent of delocalization in polymers well and employs 20% Hartree-Fock exchange and $\omega = 0.2 \text{ bohr}^{-1}$.

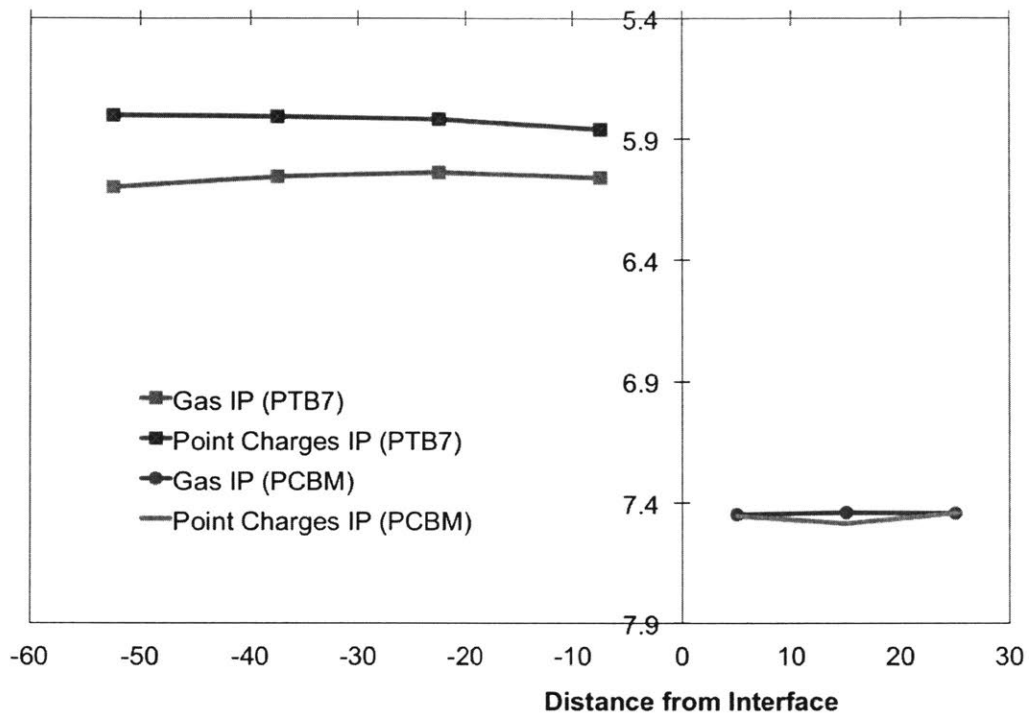


Figure 5-2: Graph of the IP values in PTB7 as a function of distance from the interface in PCBM. Data computed absent of the molecular environment is labeled 'gas' and is red for the hole and blue for the electron. Data computed with the surrounding molecules represented by their point charges is labeled 'point charges' and colored green for the hole and magenta for the electron.

5.3 Results and Discussion

Interfacial Electronic Structure

Shown in Figure 5-2 and 5-3 are the interfacial IP and EA values for both the PTB7 and PCBM phases as a function of distance from the interface.

Hole Delocalization

To analyze the extent of delocalization, we employ the inverse participation ratio:

$$IPR = \frac{1}{\sum_{i \in Sites} (P_i)^2} \quad (5.1)$$

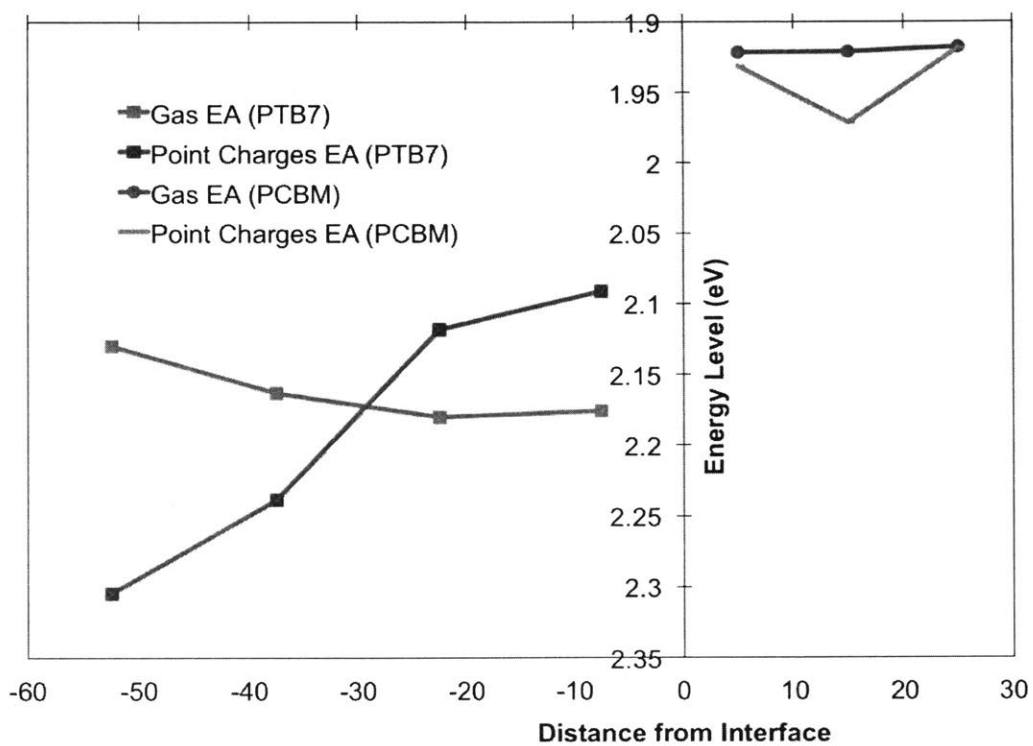


Figure 5-3: Graph of the EA values in PTB7 as a function of distance from the interface in PCBM. Data computed absent of the molecular environment is labeled 'gas' and is red for the hole and blue for the electron. Data computed with the surrounding molecules represented by their point charges is labeled 'point charges' and colored green for the hole and magenta for the electron.

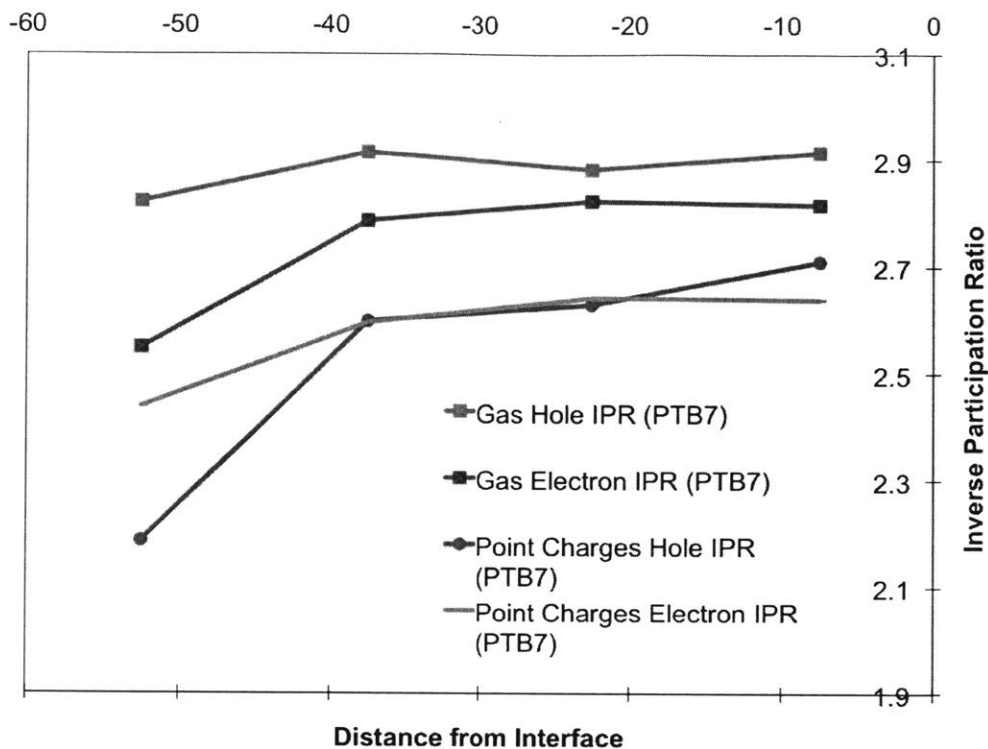


Figure 5-4: Graph of the IPR values for the states in PTB7 as a function of distance from the interface in PCBM. Data computed absent of the molecular environment is labeled 'gas' and is red for the hole and blue for the electron. Data computed with the surrounding molecules represented by their point charges is labeled 'point charges' and colored green for the hole and magenta for the electron.

where P_i is the population on site i . For sites we use the Mulliken charge on each of the 6 monomeric units, taking the difference between the cationic and neutrally charged molecule for the hole calculation and the anionic and neutral for the electron. The motivation behind the coarse-graining is to avoid well-known issues with Mulliken charges' spurious charge assignment []. We have successfully used this metric in previous studies on polymeric systems []. The computed IPR values of the hole states in PTB7 are plotted in figure 5-4.

5.4 Conclusion

In this study, we have found that

What we have found here implies

Future studies on

5.5 Acknowledgements

This work was funded by ENI S.p.A. as part of the MIT Energy Initiative.

Chapter 6

Optimal Tuning in Machine Learning

6.1 Introduction

In recent years, machine learning has risen in prominence as a useful tool for quantum chemistry problems. It has found applications in various domains: molecular rational design[126], construction of many-body force fields[127], augmentation of electronic structure methods[128], and more[129]. For rational design in particular, great advances have been made in the past few years in transforming molecular graphs into a fixed-length vector that can then be readily used for high-throughput screening[130]. This has been demonstrated recently in accelerated explorations of molecular space for novel organic light-emitting diodes [126] and solar cells [131].

For many molecular applications, excited state properties are critical for device performance. The most commonly-used excited state method is time-dependent density functional theory (TDDFT) [132]. However, TDDFT generally has accuracy of around 0.3 eV [133], in addition to critical failure modes involving charge-transfer states [134]. These can be partially remedied through the use of optimally-tuned range-separated functionals (OTRS) [135]. OTRS functionals are costly because they require the performance of many successive density-functional calculations to compute the range-separation parameter. This multiplies the cost usually by around 10-30 times, making it unfeasible for high-throughput screening or dynamics calculations.

Herein, we present a method for computing an approximate range-separation pa-

parameter using a neural-network fingerprint. Because optimal tuning is completely *ab initio* method, we can compute these parameters for a large set of molecules, enabling us to effectively train a neural network. We show that we can recover OTRS-quality results at a fraction of the cost, allowing high-throughput rational design to use optimal tuning. Additionally, we discuss the distributions of range-separation parameters for the datasets we use and suggest ways of exploiting and interpreting their statistics.

6.2 Methods

We employed the neural fingerprinting method described in Duvenaud et. al. [136] on a database of 4000 molecules taken from two sources: the 6-element members of GDB-11 [137] and 2000 randomly sampled molecules from the Harvard Clean Energy Project [1]. We divide our data set into halves, with one half used as the training set and the other half used as the test set. We optimized hyperparameters the same way as Duvenaud et. al. [136], and use a single-layer network to convert the fingerprint into a range-separation value.

We used RDKit to construct xyz coordinates from the SMILES strings [138]. Following Refaely-Abramson et. al., we then computed the range-separation values [135]. One important thing to note about this methodology is that it employs no input from experiment and therefore can be extended to an arbitrarily large data set.

6.3 Results and Discussion

We show how our model performs in Figure 6-1. We predict the optimal tuning parameters for species in our test set with a mean absolute error of 0.015 bohr^{-1} .

The distributions of the range-separation values of the two databases we use are given in Figure 6-2. We find that the distributions are very narrow and well-separated, likely due to the disjoint distributions of molecular sizes, as the optimal range-separation parameter is quite sensitive to the extent of the electronic system [135]. This is a plausible explanation for the success of our model. However, this

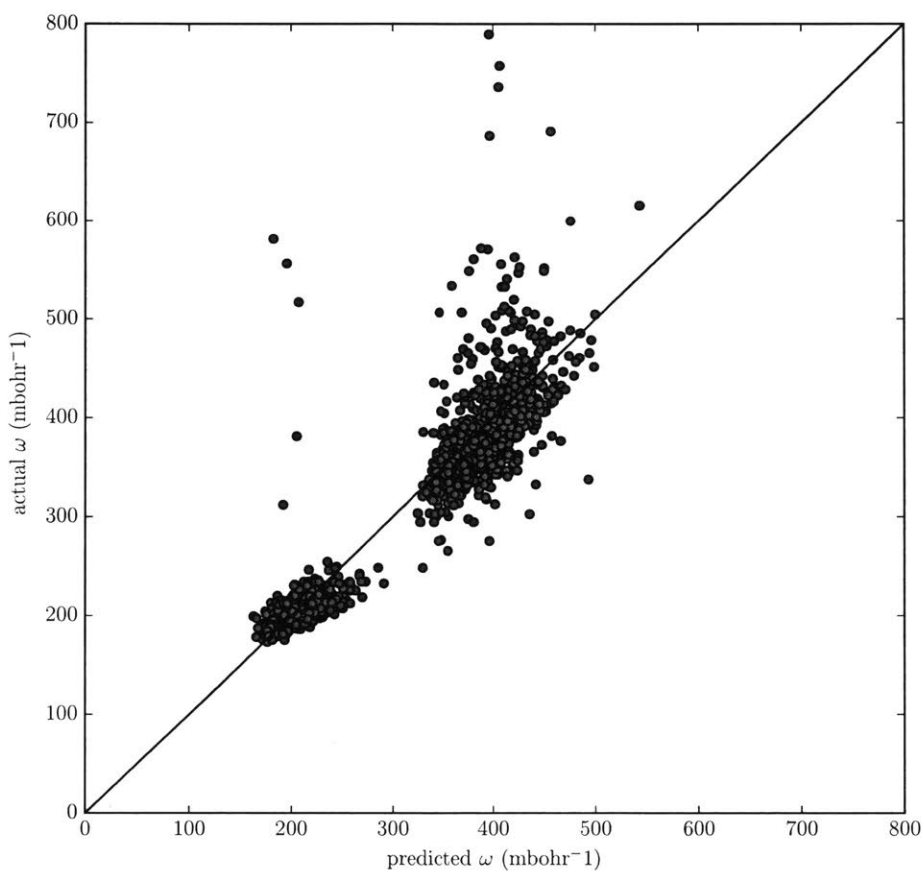


Figure 6-1: Plot comparing the predicted ω values with the exact ones. We reproduce the true optimal values with a mean absolute error of 0.015 bohr^{-1} .

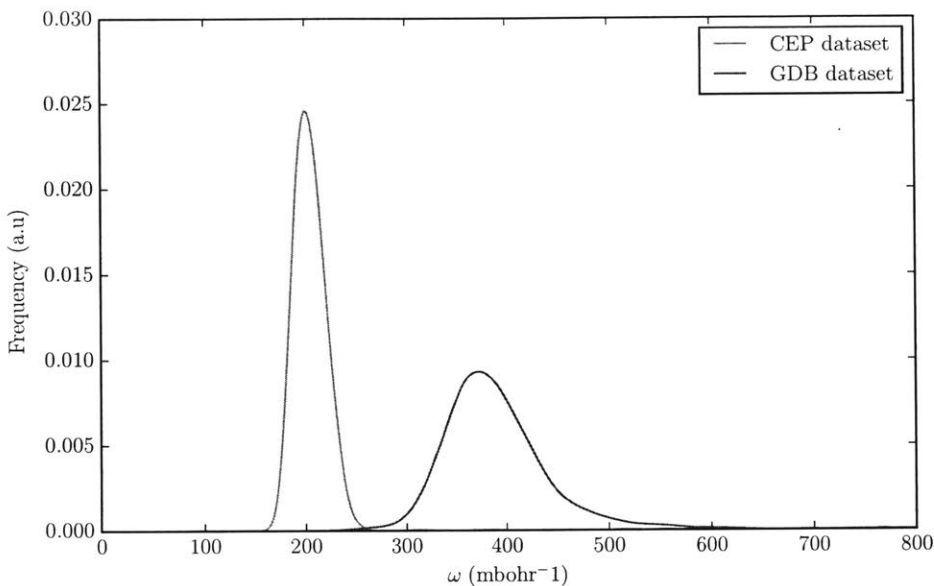


Figure 6-2: The distribution of true omega values for the two databases employed in this study. We find that they have little overlap, demonstrating how each one only samples a limited region of ω space.

also suggests that a viable strategy for optimal tuning within similar high-throughput screening databases is simply to use the average of a small sample of species, as the intra-database variation is quite small. One interesting critique that emerges here is that although these databases are supposed to span a large chemical space, from a range-separation perspective the databases are quite homogeneous.

To discuss the correlation between the molecular size and the optimal range-separation value, we plot in Figure 6-3 the relationship between the characteristic radius of a molecule (the standard deviation of the distance between atomic positions and the mean atomic position) and its OTRS value. Refaely-Abramson and coworkers examined how the optimal ω value is strongly determined by the molecule’s characteristic radius, which led us to suspect that our neural net was only picking up on that aspect of the molecule. However, upon examination of our databases, we find little correlation between molecular radius and the optimal ω value, despite our databases spanning a very large range of characteristic radii. This suggests that our neural network is picking up on something more subtle than the molecular radius, as that

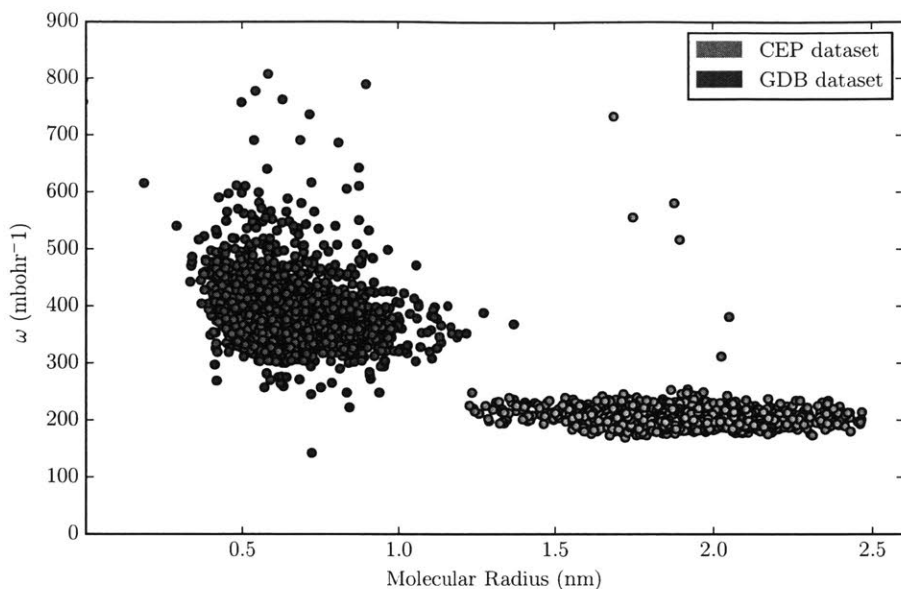


Figure 6-3: The distribution of true omega values for the two databases employed in this study, plotted versus the molecule’s characteristic radius.

would not be a useful metric.

6.4 Conclusions

We have shown that the cost of optimal tuning can be greatly reduced through the use of a neural network to provide an approximately optimal range-separation value. This can greatly accelerate high-throughput screening efforts that need optimally-tuned quality results. We also suggest the use of other simple models to capture the variation in the optimal range-separation value without the full optimization procedure. Future work can focus on extending these simple models by looking at molecular features that are strongly correlated with the optimal range-separation parameters or on the usage of other optimal tuning schemes.

Chapter 7

Conclusion

My only regret is that I have only one half-decade to give to my degree. There are plenty of unanswered questions lurking here that remain for my successors.

The most pressing is applying and extending what I've learned about internal conversion and intersystem crossing rate predictions. This is the field I've worked in where people understand the least and the questions that need answering are manifestly important: these non-radiative decay pathways directly impact the efficiency of organic devices. Because the applications are so broad and the understanding so shallow, this is where I would direct future students in need of a project.

That said, my other work on the interfacial band levels in bulk heterojunction devices and predicting optimal tuning parameters with machine learning is useful, still. However, it seems likely that the use will decay in the immediate future. Less and less attention is being paid to bulk heterojunctions recently as attention redirects to perovskite devices. Although an understanding of interfacial band levels in disordered materials will likely be useful for future technologies, the work I've done is hardly the first in the field (nor is it likely to be the last). Optimal tuning parameter prediction is useful and charming, but again it seems likely that it has an expiration date. Machine learning of the sort used to predict the optimal range-separation parameters seems likely to go after electron structure calculations in a more hands-on fashion than merely modifying functionals. If successful, that will make obsolete the work shown here.

My only additional advice to the future generation is to read widely and well. Be skeptical of papers - people rarely know what they claim to know and a critical eye, as well as an understanding of the literature, will help you identify this.

Bibliography

- [1] J. Cornil, S. Verlaak, N. Martinelli, A. Mityashin, Y. Olivier, T. Van Rege-morter, G. D'Avino, L. Muccioli, C. Zannoni, F. Castet, D. Beljonne, and P. Heremans. Exploring the energy landscape of the charge transport levels in organic semiconductors at the molecular scale. *Accounts of Chemical Research*, 46(2):434–443, 2013.
- [2] Frédéric Castet, Gabriele D'Avino, Luca Muccioli, Jérôme Cornil, and David Beljonne. Charge separation energetics at organic heterojunctions: on the role of structural and electrostatic disorder. *Phys. Chem. Chem. Phys.*, 16(38):20279–20290, oct 2014.
- [3] Heinz Bässler and Anna Köhler. "Hot or cold": how do charge transfer states at the donor-acceptor interface of an organic solar cell dissociate? *Phys. Chem. Chem. Phys.*, 17(43):28451–28462, 2015.
- [4] David P. McMahon, David L. Cheung, and Alessandro Troisi. Why holes and electrons separate so well in polymer/fullerene photovoltaic cells. *Journal of Physical Chemistry Letters*, 2(21):2737–2741, 2011.
- [5] Shane R. Yost and Troy Van Voorhis. Electrostatic effects at organic semiconductor interfaces: A mechanism for "cold" exciton breakup. *Journal of Physical Chemistry C*, 117(11):5617–5625, 2013.
- [6] John E. Anthony. Functionalized acenes and heteroacenes for organic electronics. *Chemical Reviews*, 106(12):5028–5048, 2006.
- [7] Michael Bendikov, Fred Wudl, and Dmitrii F. Perepichka. *Tetrathiafulvalenes, oligoacenes, and their buckminsterfullerene derivatives: The brick and mortar of organic electronics*, volume 104. 2004.
- [8] John E. Anthony, Antonio Facchetti, Martin Heeney, Seth R. Marder, and Xiaowei Zhan. N-Type organic semiconductors in organic electronics. *Advanced Materials*, 22(34):3876–3892, 2010.
- [9] Stephen R. Forrest, Donal D C Bradley, and Mark E. Thompson. Measuring the efficiency of organic light-emitting devices. *Advanced Materials*, 15(13):1043–1048, 2003.

- [10] Jonathan D. Servaites, Mark A. Ratner, and Tobin J. Marks. Practical efficiency limits in organic photovoltaic cells: Functional dependence of fill factor and external quantum efficiency. *Applied Physics Letters*, 95(16):2009–2011, 2009.
- [11] Ji-Yun Hu, Yingying Ning, Yin-Shan Meng, Jing Zhang, Zhuo-Yan Wu, Song Gao, and Jun-Long Zhang. Highly Near-IR-Emissive Ytterbium(III) Complexes with Unprecedented Quantum Yields. *Chem. Sci.*, 2017.
- [12] Marc Vendrell, Duanting Zhai, Jun Cheng Er, and Young Tae Chang. Combinatorial strategies in fluorescent probe development. *Chemical Reviews*, 112(8):4391–4420, 2012.
- [13] J Zhang, R E Campbell, A Y Ting, A Y Ting, and R Y Tsien. Creating new fluorescent probes for cell biology. *Nature Reviews Molecular Cell Biology*, 3(12):906–918, 2002.
- [14] Panče Naumov, Yutaka Ozawa, Kei Ohkubo, and Shunichi Fukuzumi. Structure and spectroscopy of oxyluciferin, the light emitter of the firefly bioluminescence. *Journal of the American Chemical Society*, 131(32):11590–11605, 2009.
- [15] Mohammad R Momeni and Alex Brown. A Local CC2 and TDA-DFT Double Hybrid Study on BODIPY/aza-BODIPY Dimers as Heavy Atom Free Triplet Photosensitizers for Photodynamic Therapy Applications. *Journal of Physical Chemistry A*, 120(16):2550–2560, 2016.
- [16] R. F. Kubin and A. N. Fletcher. Fluorescence quantum yields of some rhodamine dyes. *Journal of Luminescence*, 27(4):455–462, 1982.
- [17] Guiford Jones II, William R Jackson, and Arthur M Halpern. Medium Effects on Fluorescence Quantum Yields and Lifetimes for Coumarin Laser-Dyes. *Chem. Phys. Lett.*, 72(2):391–395, 1980.
- [18] Nicholas J. Turro. *Modern molecular photochemistry*. 1991.
- [19] Robert Englman and Joshua Jortner. The energy gap law for radiationless transitions in large molecules. *Molecular Physics*, 18(2):145–164, feb 1970.
- [20] Veeradej Chynwat and Harry A. Frank. The application of the energy gap law to the S1 energies and dynamics of carotenoids. *Chemical Physics*, 194(2-3):237–244, 1995.
- [21] D Gosztola, M P Niemczyk, W Svec, a S Lukas, and M R Wasielewski. Excited doublet states of electrochemically generated aromatic imide and diimide radical anions. *Journal of Physical Chemistry A*, 104(28):6545–6551, 2000.
- [22] Gilles Ulrich, Raymond Ziessel, and Anthony Harriman. The chemistry of fluorescent bodipy dyes: Versatility unsurpassed. *Angewandte Chemie - International Edition*, 47(7):1184–1201, 2008.

- [23] Joseph E. Bullock, Michael T. Vagnini, Charusheela Ramanan, Dick T. Co, Thea M. Wilson, Jay W. Dicke, Tobin J. Marks, and Michael R. Wasielewski. Photophysics and redox properties of rylene imide and diimide dyes alkylated ortho to the imide groups. *Journal of Physical Chemistry B*, 114(5):1794–1802, 2010.
- [24] Gonzalo Duran-Sampedro, Antonia R. Agarrabeitia, Inmaculada Garcia-Moreno, Angel Costela, Jorge Bañuelos, Teresa Arbeloa, Iñigo López Arbeloa, Jose Luis Chiara, and María J. Ortiz. Chlorinated BODIPYs: Surprisingly efficient and highly photostable laser dyes. *European Journal of Organic Chemistry*, (32):6335–6350, 2012.
- [25] Ixone Esnal, Arlette Urías-Benavides, C. F. Azael Gómez-Durán, Carlos A. Osorio-Martínez, Inmaculada García-Moreno, Angel Costela, Jorge Bañuelos, Nerea Epelde, Iñigo López Arbeloa, Rongrong Hu, Ben Zhong Tang, and Eduardo Peña-Cabrera. Reaction of amines with 8-methylthioBODIPY: Dramatic optical and laser response to amine substitution. *Chemistry - An Asian Journal*, 8(11):2691–2700, 2013.
- [26] Benjamin G Levine and Todd J Martínez. Isomerization Through Conical Intersections. *Annual Review of Physical Chemistry*, 58(1):613–634, 2007.
- [27] Raúl Montero, Álvaro Peralta Conde, Virginia Ovejas, Fernando Castaño, and Asier Longarte. Ultrafast photophysics of the isolated indole molecule. In *Journal of Physical Chemistry A*, 2012.
- [28] Matthias Ruckebauer, Mario Barbatti, Thomas Müller, and Hans Lischka. Nonadiabatic photodynamics of a retinal model in polar and nonpolar environment. *Journal of Physical Chemistry A*, 2013.
- [29] Felix Plasser, Rachel Crespo-Otero, Marek Pederzoli, Jiri Pittner, Hans Lischka, and Mario Barbatti. Surface Hopping Dynamics with Correlated Single-Reference Methods: 9H-Adenine as a Case Study. *Journal of Chemical Theory and Computation*, 10(4):1395–1405, 2014.
- [30] Zhongneng Zhou, Xueyao Zhou, Xueli Wang, Bin Jiang, Yongle Li, Jinquan Chen, and Jianhua Xu. Ultrafast Excited-State Dynamics of Cytosine Aza-Derivative and Analogues. *The Journal of Physical Chemistry A*, 121(14):2780–2789, 2017.
- [31] Angelo Giussani, Manuela Merchán, João Paulo Gobbo, and Antonio Carlos Borin. Relaxation mechanisms of 5-azacytosine. *Journal of Chemical Theory and Computation*, 10(9):3915–3924, 2014.
- [32] Akira Nakayama, Shohei Yamazaki, and Tetsuya Taketsugu. Quantum chemical investigations on the nonradiative deactivation pathways of cytosine derivatives. *Journal of Physical Chemistry A*, 118(40):9429–9437, 2014.

- [33] Nina Ismail, Lluís Blancafort, Massimo Olivucci, Bern Kohler, and Michael A Robb. Ultrafast decay of electronically excited singlet cytosine via a π, π^* to $n0, \pi^*$ state switch. *Journal of the American Chemical Society*, 124(24):6818–6819, 2002.
- [34] Shohei Yamazaki and Shigeki Kato. Solvent Effect on Conical Intersections in Excited-State 9H-Adenine: Radiationless Decay Mechanism in Polar Solvent.
- [35] I V Polyakov, B L Grigorenko, E M Epifanovsky, A I Krylov, and A V Nemukhin. Potential energy landscape of the electronic states of the GFP chromophore in different protonation forms: Electronic transition energies and conical intersections. *Journal of Chemical Theory and Computation*, 6(8):2377–2387, 2010.
- [36] Lara Martínez-Fernández, Inés Corral, Giovanni Granucci, and Maurizio Persico. Competing ultrafast intersystem crossing and internal conversion: a time resolved picture for the deactivation of 6-thioguanine. *Chemical Science*, 5(4):1336, 2014.
- [37] Theis I. Sølling, Thomas S. Kuhlman, Anne B. Stephansen, Liv B. Klein, and Klaus B. Møller. The non-ergodic nature of internal conversion. *ChemPhysChem*, 15(2):249–259, 2014.
- [38] B Amand and R Bensasson. Determination of triplet quantum yields by laser flash absorption spectroscopy. *Physics Letters*, 34(1), 1975.
- [39] Jimena S. Zugazagoitia, César Xavier Almora-Díaz, and Jorge Peon. Ultrafast intersystem crossing in 1-nitronaphthalene. An experimental and computational study. *Journal of Physical Chemistry A*, 112(3):358–365, 2008.
- [40] Christel M. Marian. Spin-orbit coupling and intersystem crossing in molecules. *Wiley Interdisciplinary Reviews: Computational Molecular Science*, 2(2):187–203, mar 2012.
- [41] Qian Peng, Yingli Niu, Chunmei Deng, and Zhigang Shuai. Vibration correlation function formalism of radiative and non-radiative rates for complex molecules. *Chemical Physics*, 370(1-3):215–222, 2010.
- [42] Isadore B. Berlman. 6- $\{GRAPHIS\}$. In Isadore B. Berlman, editor, *Handbook of Fluorescence Spectra of Aromatic Molecules*, pages 107–415. Academic Press, 2nd edition, 1971.
- [43] Kengo Suzuki, Attila Demeter, Wolfgang Kühnle, Erich Tauer, Klaas A. Zachariasse, Seiji Tobita, and Haruo Shizuka. Internal conversion in 4-substituted 1-naphthylamines. influence of the electron donor/acceptor substituent character. 2:981–991, 2000.

- [44] Kazuyuki Takehira, Kengo Suzuki, Hiroshi Hiratsuka, and Seiji Tobita. Fast internal conversion in 1-(dimethylamino)naphthalene: Effects of methoxy substitution on the naphthalene ring. 413(1-3):52–58, 2005.
- [45] Ingo Rückert, Attila Demeter, Olaf Morawski, Wolfgang Kühnle, Erich Tauer, and Klaas A. Zachariasse. Internal conversion in 1-aminonaphthalenes. influence of amino twist angle. 103(13):1958–1966, 1999.
- [46] Isadore B. Berlman. 4-{COMPOUNDS}. In Isadore B. Berlman, editor, *Handbook of Fluorescence Spectra of Aromatic Molecules*, pages 67–95. Academic Press, 2nd edition, 1971.
- [47] So Hirata and Martin Head-Gordon. Time-dependent density functional theory within the tamm–dancoff approximation. 314(3-4):291–299, 1999.
- [48] Raúl Montero, Asier Longarte, Álvaro Peralta Conde, Carolina Redondo, Fernando Castaño, Israel González-Ramírez, Angelo Giussani, Luis Serrano-Andrés, and Manuela Merchán. Photophysics of 1-aminonaphthalene: A theoretical and time-resolved experimental study. 113(48):13509–13518, 2009.
- [49] Benjamin G. Levine, Joshua D. Coe, and Todd J. Martínez. Optimizing conical intersections without derivative coupling vectors: Application to multistate multireference second-order perturbation theory (ms-caspt2). 112(2):405–413, 2008.
- [50] Xing Zhang and John M. Herbert. Excited-state deactivation pathways in uracil versus hydrated uracil: Solvatochromatic shift in the $1n\pi^*$ state is the key. 118(28):7806–7817, 2014.
- [51] Y. Shao, Z. Gan, E. Epifanovsky, A. T. B. Gilbert, M. Wormit, J. Kussmann, A. W. Lange, A. Behn, J. Deng, X. Feng, D. Ghosh, M. Goldey, P. R. Horn, L. D. Jacobson, I. Kaliman, R. Z. Khaliullin, T. Kús, A. Landau, J. Liu, E. I. Proynov, Y. M. Rhee, R. M. Richard, M. A. Rohrdanz, R. P. Steele, E. J. Sundstrom, H. L. Woodcock III, P. M. Zimmerman, D. Zuev, B. Albrecht, E. Alguire, B. Austin, G. J. O. Beran, Y. A. Bernard, E. Berquist, K. Brandhorst, K. B. Bravaya, S. T. Brown, D. Casanova, C.-M. Chang, Y. Chen, S. H. Chien, K. D. Closser, D. L. Crittenden, M. Diedenhofen, R. A. DiStasio Jr., H. Dop, A. D. Dutoi, R. G. Edgar, S. Fatehi, L. Fusti-Molnar, A. Ghysels, A. Golubeva-Zadorozhnaya, J. Gomes, M. W. D. Hanson-Heine, P. H. P. Harbach, A. W. Hauser, E. G. Hohenstein, Z. C. Holden, T.-C. Jagau, H. Ji, B. Kaduk, K. Khistyayev, J. Kim, J. Kim, R. A. King, P. Klunzinger, D. Kosenkov, T. Kowalczyk, C. M. Krauter, K. U. Lao, A. Laurent, K. V. Lawler, S. V. Levchenko, C. Y. Lin, F. Liu, E. Livshits, R. C. Lochan, A. Luenser, P. Manohar, S. F. Manzer, S.-P. Mao, N. Mardirossian, A. V. Marenich, S. A. Maurer, N. J. Mayhall, C. M. Oana, R. Olivares-Amaya, D. P. O’Neill, J. A. Parkhill, T. M. Perrine, R. Peverati, P. A. Pieniazek, A. Prociuk, D. R. Rehn, E. Rosta, N. J. Russ, N. Sergueev, S. M. Sharada, S. Sharma, D. W.

- Small, A. Sodt, T. Stein, D. Stück, Y.-C. Su, A. J. W. Thom, T. Tsuchimochi, L. Vogt, O. Vydrov, T. Wang, M. A. Watson, J. Wenzel, A. White, C. F. Williams, V. Vanovschi, S. Yeganeh, S. R. Yost, Z.-Q. You, I. Y. Zhang, X. Zhang, Y. Zhou, B. R. Brooks, G. K. L. Chan, D. M. Chipman, C. J. Cramer, W. A. Goddard III, M. S. Gordon, W. J. Hehre, A. Klamt, H. F. Schaefer III, M. W. Schmidt, C. D. Sherrill, D. G. Truhlar, A. Warshel, X. Xua, A. Aspuru-Guzik, R. Baer, A. T. Bell, N. A. Besley, J.-D. Chai, A. Dreuw, B. D. Dunietz, T. R. Furlani, S. R. Gwaltney, C.-P. Hsu, Y. Jung, J. Kong, D. S. Lambrecht, W. Liang, C. Ochsenfeld, V. A. Rassolov, L. V. Slipchenko, J. E. Subotnik, T. Van Voorhis, J. M. Herbert, A. I. Krylov, P. M. W. Gill, and M. Head-Gordon. Advances in molecular quantum chemistry contained in the q-chem 4 program package. 113:184–215, 2015.
- [52] A. F. van Driel, G. Allan, C. Delerue, P. Lodahl, W. L. Vos, and D. Vanmaekelbergh. Frequency-dependent spontaneous emission rate from cdse and cdte nanocrystals: Influence of dark states. 95:236804, Dec 2005.
- [53] Michael Kasha. Characterization of electronic transitions in complex molecules. 9:14–19, 1950.
- [54] S. E. Braslavsky. Glossary of terms used in photochemistry, 3rd edition (iupac recommendations 2006). 79(4):293–465, 2007.
- [55] Stephen R. Forrest. The path to ubiquitous and low-cost organic electronic appliances on plastic. *Nature*, 428(6986):911–918, 2004.
- [56] Gang Li, Rui Zhu, and Yang Yang. Polymer solar cells. *Nature Photonics*, 6(3):153–161, 2012.
- [57] Huawei Hu, Kui Jiang, Guofang Yang, Jing Liu, Zhengke Li, Haoran Lin, Yuhang Liu, Jingbo Zhao, Jie Zhang, Fei Huang, Yongquan Qu, Wei Ma, and He Yan. Terthiophene-based D-A polymer with an asymmetric arrangement of alkyl chains that enables efficient polymer solar cells. *Journal of the American Chemical Society*, 137(44):14149–14157, 2015.
- [58] Jing De Chen, Chaohua Cui, Yan Qing Li, Lei Zhou, Qing Dong Ou, Chi Li, Yongfang Li, and Jian Xin Tang. Single-junction polymer solar cells exceeding 10% power conversion efficiency. *Advanced Materials*, 27(6):1035–1041, 2015.
- [59] Letian Dou, Jingbi You, Ziruo Hong, Zheng Xu, Gang Li, Robert A. Street, and Yang Yang. 25th anniversary article: A decade of organic/polymeric photovoltaic research. *Advanced Materials*, 25(46):6642–6671, 2013.
- [60] Jenny Nelson. The Physics of Solar Cells. *Properties of Semiconductor Materials*, page 384, 2003.
- [61] Carsten Deibel and Vladimir Dyakonov. Polymer-Fullerene Bulk Heterojunction Solar Cells. *Rep. Prog. Phys.*, 73(9):1–39, 2010.

- [62] J. J. M. Halls, C. A. Walsh, N. C. Greenham, E. A. Marseglia, R. H. Friend, S. C. Moratti, and A. B. Holmes. Efficient photodiodes from interpenetrating polymer networks, aug 1995.
- [63] G. Yu, J. Gao, J. C. Hummelen, F. Wudl, and A. J. Heeger. Polymer Photovoltaic Cells: Enhanced Efficiencies via a Network of Internal Donor-Acceptor Heterojunctions. *Science*, 270(5243):1789–1791, 1995.
- [64] Xiaoni Yang, Joachim Loos, Sjoerd C. Veenstra, W. J H Verhees, Martijn M. Wienk, Jan M. Kroon, M. A J Michels, and R. A J Janssen. Nanoscale morphology of high-performance polymer solar cells. *Nano Letters*, 5(4):579–583, 2005.
- [65] Barry P. Rand, Diana P. Burk, and Stephen R. Forrest. Offset energies at organic semiconductor heterojunctions and their influence on the open-circuit voltage of thin-film solar cells. *Physical Review B - Condensed Matter and Materials Physics*, 75(11):1–11, 2007.
- [66] X. Y. Zhu, Q. Yang, and M. Muntwiler. Charge-transfer excitons at organic semiconductor surfaces and interfaces. *Accounts of Chemical Research*, 42(11):1779–1787, 2009.
- [67] Sung Heum Park, Mario Leclerc, Alan J. Heeger, and Kwanghee Lee. High efficiency polymer solar cells with internal quantum efficiency approaching 100%. *Proceedings of SPIE*, 7416(May 2011):74160P–74160P–10, 2009.
- [68] Sheridan Few, Jarvist M. Frost, and Jenny Nelson. Models of charge pair generation in organic solar cells. *Phys. Chem. Chem. Phys.*, 17(4):2311–2325, 2015.
- [69] Bernard Kippelen and Jean-Luc Brédas. Organic photovoltaics. *Energy & Environmental Science*, 2(3):251, 2009.
- [70] Artem A. Bakulin, Stoichko D. Dimitrov, Akshay Rao, Philip C Y Chow, Christian B. Nielsen, Bob C. Schroeder, Iain McCulloch, Huib J. Bakker, James R. Durrant, and Richard H. Friend. Charge-transfer state dynamics following hole and electron transfer in organic photovoltaic devices. *Journal of Physical Chemistry Letters*, 4(1):209–215, 2013.
- [71] Stoichko D Dimitrov, Artem a Bakulin, Christian B Nielsen, Bob Camille Schroeder, Junping Du, Hugo Bronstein, Iain Mcculloch, Richard H Friend, James R Durrant, and Bob C Schroeder. On the Energetic Dependence of Charge Separation in Low Bandgap Polymer / Fullerene Blends On the Energetic Dependence of Charge Separation in Low Bandgap Polymer / Fullerene Blends. *Journal of the American Chemical Society*, pages 10–13, 2012.

- [72] Askat E. Jailaubekov, Adam P. Willard, John R. Tritsch, Wai-Lun Chan, Na Sai, Raluca Gearba, Loren G. Kaake, Kenrick J. Williams, Kevin Leung, Peter J. Rossky, and X-Y. Zhu. Hot charge-transfer excitons set the time limit for charge separation at donor/acceptor interfaces in organic photovoltaics. *Nature Materials*, 12(1):66–73, 2012.
- [73] Hiroyuki Tamura and Irene Burghardt. Ultrafast charge separation in organic photovoltaics enhanced by charge delocalization and vibronically hot exciton dissociation. *Journal of the American Chemical Society*, 135(44):16364–16367, 2013.
- [74] Xingxing Shen, Guangchao Han, Di Fan, Yujun Xie, and Yuanping Yi. Hot charge-transfer states determine exciton dissociation in the DTD-CTB/C₆₀ complex for organic solar cells: A theoretical insight. *Journal of Physical Chemistry C*, 119(21):11320–11326, 2015.
- [75] Hideo Ohkita, Steffan Cook, Yeni Astuti, Warren Duffy, Steve Tierney, Weimin Zhang, Martin Heeney, Iain McCulloch, Jenny Nelson, Donal D.C. Bradley, and James R. Durrant. Charge carrier formation in polythiophene/fullerene blend films studied by transient absorption spectroscopy. *Journal of the American Chemical Society*, 130(10):3030–3042, 2008.
- [76] Stoichko D. Dimitrov and James R. Durrant. Materials design considerations for charge generation in organic solar cells. *Chemistry of Materials*, 26(1):616–630, 2014.
- [77] Jiye Lee, Koen Vandewal, Shane R. Yost, Matthias E. Bahlke, Ludwig Goris, Marc A. Baldo, Jean V. Manca, and Troy Van Voorhis. Charge transfer state versus hot exciton dissociation in polymer-fullerene blended solar cells. *Journal of the American Chemical Society*, 132(34):11878–11880, 2010.
- [78] Koen Vandewal, Steve Albrecht, Eric T. Hoke, Kenneth R. Graham, Johannes Widmer, Jessica D. Douglas, Marcel Schubert, William R. Mateker, Jason T. Bloking, George F. Burkhard, Alan Sellinger, Jean M. J. Fréchet, Aram Amassian, Moritz K. Riede, Michael D. McGehee, Dieter Neher, and Alberto Salleo. Efficient charge generation by relaxed charge-transfer states at organic interfaces. *Nature Materials*, 13(1):63–68, 2013.
- [79] Bhoj R. Gautam, Robert Younts, Wentao Li, Liang Yan, Evgeny Danilov, Erik Klump, Iordania Constantinou, Franky So, Wei You, Harald Ade, and Kenan Gundogdu. Charge Photogeneration in Organic Photovoltaics: Role of Hot versus Cold Charge-Transfer Excitons. *Advanced Energy Materials*, 6(1):1–6, 2016.
- [80] Jean Luc Brédas, Joseph E. Norton, Jérôme Cornil, and Veaceslav Coropceanu. Molecular understanding of organic solar cells: The challenges. *Accounts of Chemical Research*, 42(11):1691–1699, 2009.

- [81] Brett M. Savoie, Akshay Rao, Artem A. Bakulin, Simon Gelinas, Bijan Movaghar, Richard H. Friend, Tobin J. Marks, and Mark A. Ratner. Unequal partnership: Asymmetric roles of polymeric donor and fullerene acceptor in generating free charge. *Journal of the American Chemical Society*, 136(7):2876–2884, 2014.
- [82] Pabitra K. Nayak, K. L. Narasimhan, and David Cahen. Separating charges at organic interfaces: Effects of disorder, hot states, and electric field. *Journal of Physical Chemistry Letters*, 4(10):1707–1717, 2013.
- [83] Bill Pandit, Nicholas E. Jackson, Tianyue Zheng, Thomas J. Fauvell, Eric F. Manley, Meghan Orr, Samantha Brown-Xu, Luping Yu, and Lin X. Chen. Molecular Structure Controlled Transitions between Free-Charge Generation and Trap Formation in a Conjugated Copolymer Series. *Journal of Physical Chemistry C*, 120(8):4189–4198, 2016.
- [84] Fiona C. Jamieson, Ester Buchaca Domingo, Thomas McCarthy-Ward, Martin Heeney, Natalie Stingelin, and James R. Durrant. Fullerenecrystallisation as a key driver of charge separation in polymer/fullerene bulk heterojunction solar cells. *Chem. Sci.*, 3(2):485–492, 2012.
- [85] Girish Lakhwani, Akshay Rao, and Richard H. Friend. Bimolecular Recombination in Organic Photovoltaics. *Annual Review of Physical Chemistry*, 65(1):557–581, 2014.
- [86] Peter Peumans, Soichi Uchida, and Stephen R. Forrest. Efficient bulk heterojunction photovoltaic cells using small-molecular-weight organic thin films. *Nature*, 425(6954):158–162, 2003.
- [87] Ester Buchaca-Domingo, Koen Vandewal, Zhuping Fei, Scott E. Watkins, Fiona H. Scholes, James H. Bannock, John C. De Mello, Lee J. Richter, Dean M. DeLongchamp, Aram Amassian, Martin Heeney, Alberto Salleo, and Natalie Stingelin. Direct correlation of charge transfer absorption with molecular donor:acceptor interfacial area via photothermal deflection spectroscopy. *Journal of the American Chemical Society*, 137(16):5256–5259, 2015.
- [88] Tao Liu, David L. Cheung, and Alessandro Troisi. Structural variability and dynamics of the P3HT/PCBM interface and its effects on the electronic structure and the charge-transfer rates in solar cells. *Phys. Chem. Chem. Phys.*, 13(48):21461–21470, 2011.
- [89] Miquel Huix-Rotllant, Hiroyuki Tamura, and Irene Burghardt. Concurrent effects of delocalization and internal conversion tune charge separation at regioregular polythiophene-fullerene heterojunctions. *Journal of Physical Chemistry Letters*, 6(9):1702–1708, 2015.

- [90] Seth Difley, Lee Ping Wang, Sina Yeganeh, Shane R. Yost, and Troy Van Voorhis. Electronic properties of disordered organic semiconductors via QM/MM simulations. *Accounts of Chemical Research*, 43(7):995–1004, jul 2010.
- [91] Shane R. Yost, Lee Ping Wang, and Troy Van Voorhis. Molecular insight into the energy levels at the organic donor/acceptor interface: A quantum mechanics/molecular mechanics study. *Journal of Physical Chemistry C*, 115(29):14431–14436, jul 2011.
- [92] Harald Hoppe and Niyazi Serdar Sariciftci. Morphology of polymer/fullerene bulk heterojunction solar cells. *J. Mater. Chem.*, 16(1):45–61, 2006.
- [93] David P. McMahon and Alessandro Troisi. Organic semiconductors: Impact of disorder at different timescales. *ChemPhysChem*, 11(10):2067–2074, 2010.
- [94] Ferdinand C. Grozema, Piet Th Van Duijnen, Yuri A. Berlin, Mark A. Ratner, and Laurens D.A. Siebbeles. Intramolecular charge transport along isolated chains of conjugated polymers: Effect of torsional disorder and polymerization defects. *Journal of Physical Chemistry B*, 106(32):7791–7795, 2002.
- [95] Manuel Schrader, Christian Körner, Chris Elschner, and Denis Andrienko. Charge transport in amorphous and smectic mesophases of dicyanovinyl-substituted oligothiophenes. *Journal of Materials Chemistry*, 22(41):22258, 2012.
- [96] Carl Poelking and Denis Andrienko. Effect of polymorphism, regioregularity and paracrystallinity on charge transport in poly(3-hexylthiophene) [P3HT] nanofibers. *Macromolecules*, 46(22):8941–8956, 2013.
- [97] Pascal Kordt, Jeroen J M Van Der Holst, Mustapha Al Helwi, Wolfgang Kowalsky, Falk May, Alexander Badinski, Christian Lennartz, and Denis Andrienko. Modeling of Organic Light Emitting Diodes: From Molecular to Device Properties. *Advanced Functional Materials*, 25(13):1955–1971, 2015.
- [98] Frédéric Laquai, Denis Andrienko, Ralf Mauer, and Paul W M Blom. Charge carrier transport and photogeneration in P3HT:PCBM photovoltaic blends. *Macromolecular Rapid Communications*, 36(11):1001–1025, 2015.
- [99] Ki Hyun Kim, Sunhee Park, Hojeong Yu, Hyunbum Kang, Inho Song, Joon Hak Oh, and Bumjoon J. Kim. Determining optimal crystallinity of diketopyrrolopyrrole-based terpolymers for highly efficient polymer solar cells and transistors. *Chemistry of Materials*, 26(24):6963–6970, 2014.
- [100] Claire H. Woo, Barry C. Thompson, Bumjoon J. Kim, Michael F. Toney, and Jean M J Fréchet. The influence of poly(3-hexylthiophene) regioregularity on fullerene-composite solar cell performance. *Journal of the American Chemical Society*, 130(48):16324–16329, 2008.

- [101] Brian A. Collins, John R. Tumbleston, and Harald Ade. Miscibility, crystallinity, and phase development in P3HT/PCBM solar cells: Toward an enlightened understanding of device morphology and stability. *Journal of Physical Chemistry Letters*, 2(24):3135–3145, 2011.
- [102] Keisuke Tajima, Yuya Suzuki, and Kazuhito Hashimoto. Polymer Photovoltaic Devices Using Fully Regioregular Poly[(2-methoxy-5-(7-dimethyloctyloxy))-1,4-phenylenevinylene]. *The Journal of Physical Chemistry C*, 112(23):8507–8510, jun 2008.
- [103] Thierry Granier, Edwin L. Thomas, David R. Gagnon, Frank E. Karasz, and Robert W. Lenz. Structure investigation of poly(p-phenylene vinylene). *Journal of Polymer Science Part B: Polymer Physics*, 24(12):2793–2804, dec 1986.
- [104] Kateri H. Dubay, Michelle Lynn Hall, Thomas F. Hughes, Chuanjie Wu, David R. Reichman, and Richard A. Friesner. Accurate force field development for modeling conjugated polymers. *Journal of Chemical Theory and Computation*, 8(11):4556–4569, nov 2012.
- [105] Jens Niklas, Kristy L. Mardis, Brian P. Banks, Gregory M. Grooms, Andreas Sperlich, Vladimir Dyakonov, Serge Beaupré, Mario Leclerc, Tao Xu, Luping Yu, and Oleg G. Poluektov. Highly-efficient charge separation and polaron delocalization in polymer–fullerene bulk-heterojunctions: a comparative multi-frequency EPR and DFT study. *Physical Chemistry Chemical Physics*, 15(24):9562, 2013.
- [106] Margherita Moreno, Mosè Casalegno, Guido Raos, Stefano V. Meille, and Riccardo Po. Molecular modeling of crystalline alkylthiophene oligomers and polymers. *Journal of Physical Chemistry B*, 114(4):1591–1602, feb 2010.
- [107] Paolo Arosio, Margherita Moreno, Antonino Famulari, Guido Raos, Marinella Catellani, and Stefano Valdo Meille. Ordered stacking of regioregular head-to-tail polyalkylthiophenes: Insights from the crystal structure of form I' poly(3-n-butylthiophene). *Chemistry of Materials*, 21(1):78–87, jan 2009.
- [108] William L. Jorgensen, David S. Maxwell, and Julian Tirado-Rives. Development and testing of the OPLS all-atom force field on conformational energetics and properties of organic liquids. *Journal of the American Chemical Society*, 118(45):11225–11236, 1996.
- [109] Minze T Rispens, Auke Meetsma, Roman Rittberger, Christoph J Brabec, N Serdar Sariciftci, and Jan C Hummelen. Influence of the solvent on the crystal structure of PCBM and the efficiency of MDMO-PPV:PCBM 'plastic' solar cells. *Chemical communications (Cambridge, England)*, 80(17):2116–8, 2003.

- [110] David L. Cheung and Alessandro Troisi. Theoretical Study of the Organic Photovoltaic Electron Acceptor PCBM: Morphology, Electronic Structure, and Charge Localization ^{Á}. *The Journal of Physical Chemistry C*, 114(48):20479–20488, dec 2010.
- [111] David M. Huang, Roland Faller, Khanh Do, and Adam J. Moule. Coarse-grained computer simulations of polymer/fullerene bulk heterojunctions for organic photovoltaic applications. *Journal of Chemical Theory and Computation*, 6(2):526–537, feb 2010.
- [112] B Hess, C Kutzner, D van der Spoel, and E Lindahl. GROMACS 4: algorithms for highly efficient, load balanced, and scalable molecular simulations. *J. Chem. Theory and Comput.*, 4(3):435–447, 2008.
- [113] William Humphrey, Andrew Dalke, and Klaus Schulten. {VMD}: {Visual} molecular dynamics. *Journal of Molecular Graphics*, 14(1):33–38, 1996.
- [114] Mary A. Rohrdanz, Katie M. Martins, and John M. Herbert. A long-range-corrected density functional that performs well for both ground-state properties and TD-DFT excitation energies, including charge-transfer excited states. *Journal of Chemical Physics*, 130(5):054112, 2009.
- [115] Yihan Shao and Et. Al. Advances in molecular quantum chemistry contained in the Q-Chem 4 program package. *Molecular Physics*, 113(2):184–215, 2015.
- [116] Nan Shao and Qin Wu. Charge self-localization in π -conjugated polymers by long range corrected hybrid functionals. *Physical Chemistry Chemical Physics*, 16:6700, 2014.
- [117] Iffat H. Nayyar, Enrique R. Batista, Sergei Tretiak, Avadh Saxena, D. L. Smith, and Richard L. Martin. Localization of electronic excitations in conjugated polymers studied by DFT. *Journal of Physical Chemistry Letters*, 2(6):566–571, 2011.
- [118] Y Greenwald, X Xu, M Fourmigue, G Srdanov, C Koss, F Wudl, and a J Heeger. Polymer-polymer rectifying heterojunction based on poly(3,4-dicyanothiophene) and MEH-PPV. *Journal of Polymer Science Part a-Polymer Chemistry*, 36:3115–3120, 1998.
- [119] M Born. Volume and hydration warmth of ions. *Zeitschrift Fur Physik*, 1:45–48, 1920.
- [120] G. R. Hutchison, Yu-Jun Zhao, B. Delley, A. J. Freeman, M. A. Ratner, and T. J. Marks. Electronic structure of conducting polymers: Limitations of oligomer extrapolation approximations and effects of heteroatoms. *Physical Review B*, 68(3):035204, 2003.

- [121] D. L. Cheung, D. P. McMahon, and A. Troisi. A realistic description of the charge carrier wave function in microcrystalline polymer semiconductors. *Journal of the American Chemical Society*, 131(31):11179–11186, 2009.
- [122] Ting Qin and Alessandro Troisi. Relation between Structure and Electronic Properties of Amorphous MEH-PPV Polymers. *J Am Chem Soc*, 135(30):11247–11256, 2013.
- [123] William Barford, David G. Lidzey, Dmitry V. Makhov, and Anthony J.H. Meijer. Exciton localization in disordered poly(3-hexylthiophene). *Journal of Chemical Physics*, 133(4):1–7, 2010.
- [124] Sibel Leblebici, Jiye Lee, Alexander Weber-Bargioni, and Biwu Ma. Dielectric Screening to Reduce Charge Transfer State Binding Energy in Organic Bulk Heterojunction Photovoltaics. *Journal of Physical Chemistry C*, 121(6):3279–3285, 2017.
- [125] Yongye Liang, Zheng Xu, Jiangbin Xia, Szu Ting Tsai, Yue Wu, Gang Li, Claire Ray, and Luping Yu. For the bright future-bulk heterojunction polymer solar cells with power conversion efficiency of 7.4%. *Advanced Materials*, 22(20):135–138, 2010.
- [126] Rafael Gómez-Bombarelli, Jorge Aguilera-Iparraguirre, Timothy D Hirzel, David Duvenaud, Dougal Maclaurin, Martin A Blood-Forsythe, Hyun Sik Chae, Markus Einzinger, Dong-Gwang Ha, Tony Wu, Georgios Markopoulos, Soonok Jeon, Hosuk Kang, Hiroshi Miyazaki, Masaki Numata, Sunghan Kim, Wenliang Huang, Seong Ik Hong, Marc Baldo, Ryan P Adams, and Alán Aspuru-Guzik. Design of efficient molecular organic light-emitting diodes by a high-throughput virtual screening and experimental approach. *Nature Materials*, 15(10):1120–1127, 2016.
- [127] Kun Yao, John E. Herr, and John Parkhill. The many-body expansion combined with neural networks. *Journal of Chemical Physics*, 146(1), 2017.
- [128] Raghunathan Ramakrishnan, Pavlo O. Dral, Matthias Rupp, and O. Anatole Von Lilienfeld. Big data meets quantum chemistry approximations: The Δ -machine learning approach. *Journal of Chemical Theory and Computation*, 11(5):2087–2096, 2015.
- [129] Garrett B. Goh, Nathan O. Hodas, and Abhinav Vishnu. Deep learning for computational chemistry, 2017.
- [130] Justin Gilmer, Samuel S. Schoenholz, Patrick F. Riley, Oriol Vinyals, and George E. Dahl. Neural Message Passing for Quantum Chemistry. apr 2017.
- [131] Vishwesh Venkatraman, Sailesh Abburu, Bjørn Kåre Alsberg, Y. Wada, Y. Ogomi, S. Hayase, R. Katoh, T. Kaiho, T. Takahashi, A. Hagfeldt, H. Arakawa, and M. Grätzel. Artificial evolution of coumarin dyes for dye sensitized solar cells. *Phys. Chem. Chem. Phys.*, 17(41):27672–27682, 2015.

- [132] Kieron Burke, Jan Werschnik, and E. K. U. Gross. Time-dependent density functional theory: Past, present, and future. *Journal of Chemical Physics*, 123(6):062206, aug 2005.
- [133] Denis Jacquemin, Valérie Wathélet, Eric A. Perpète, and Carlo Adamo. Extensive TD-DFT benchmark: Singlet-excited states of organic molecules. *Journal of Chemical Theory and Computation*, 5(9):2420–2435, sep 2009.
- [134] Andreas Dreuw, Jennifer L. Weisman, and Martin Head-Gordon. Long-range charge-transfer excited states in time-dependent density functional theory require non-local exchange. *Journal of Chemical Physics*, 119(6):2943–2946, aug 2003.
- [135] Sivan Refaely-Abramson, Roi Baer, and Leeor Kronik. Fundamental and excitation gaps in molecules of relevance for organic photovoltaics from an optimally tuned range-separated hybrid functional. *Physical Review B - Condensed Matter and Materials Physics*, 84(7), 2011.
- [136] David Duvenaud, Dougal Maclaurin, Jorge Iparraguirre, Rafael Bombarell, Timothy Hirzel, Alan Aspuru-Guzik, and Ryan P Adams. Convolutional Networks on Graphs for Learning Molecular Fingerprints. *Advances in Neural Information Processing Systems 28*, 28:2215–2223, 2015.
- [137] Tobias Fink and Jean Louis Raymond. Virtual exploration of the chemical universe up to 11 atoms of C, N, O, F: Assembly of 26.4 million structures (110.9 million stereoisomers) and analysis for new ring systems, stereochemistry, physicochemical properties, compound classes, and drug discovery. *Journal of Chemical Information and Modeling*, 47(2):342–353, 2007.
- [138] Greg Landrum. RDKit: Open-source cheminformatics.